A Monolithic Multi-domain Hybridized Discontinuous Galerkin Solver for Inductively Coupled Plasma Flow

Nicolas Corthouts[a,b,1,*], Koen Hillewaert[a,b], Thierry Magin[c,b], Georg May[b]

[a] *Aerospace and Mechanics department, Université de Liège, Allée de la Découverte 13, 4000, Liège, Belgium*
[b] *Aeronautics and Aerospace department, von Karman Institute for Fluid Dynamics, Chaussée de Waterloo 72, 1640, Rhode-Saint-Genèse, Belgium*
[c] *Aero-Thermo-Mechanics Department, Université libre de Bruxelles, Av. Franklin Roosevelt 50, 1050, Bruxelles, Belgium*

Abstract

In the context of increasing interest in space exploration, having a reliable means of predicting the behaviour of thermal protection material during atmospheric re-entry is of capital importance. Inductively coupled plasma facilities have been designed to fulfill this demand, producing a high quality plasma and simulating accurately the re-entry conditions. In parallel, they motivated the development of dedicated efficient numerical solvers in order to better understand the experiments. However, these solvers have several drawbacks, such as slow convergence due to a staggered solution approach between the Maxwell and Navier-Stokes equations, and their use of multi-block high-quality structured mesh. In this work, we develop a novel multi-domain monolithic high-order hybridized discontinuous Galerkin (HDG) solver for inductively coupled plasma. We show that HDG method alleviates the mesh restrictions considerably, except in the boundary layer, where the mesh still needs to be structured. Moreover, we prove that the monolithic aspect of the solver allows for a fast convergence to the steady-state starting from initial data far from the solution. Using a manufactured solution, it is shown that the order of convergence of the monolithic HDG method is $p + 1$ in the L_2 norm, with p the degree of the approximation space. Finally, a comparison of the HDG code with a finite volume code (COOLFluiD) and experimental data are performed, showing a good agreement.

1. Introduction

The inductively coupled plasma (ICP) experimental facilities are very useful for space exploration. They are able to reproduce the thermodynamic conditions occurring during atmospheric reentry, allowing for the study of the thermal and chemical interaction between plasma and material (*e.g.* space debris samples, thermal protection material) with

*Corresponding author
Email addresses: ncorthouts@uliege.be (Nicolas Corthouts), Koen.Hillewaert@uliege.be (Koen Hillewaert), thierry.magin@vki.ac.be (Thierry Magin), may@aices.rwth-aachen.de (Georg May)
[1] Nicolas Corthouts is a FRIA grantee of the Fonds de la Recherche Scientifique – FNRS.

a high plasma purity and an excellent reproducibility of regimes. Pioneering work in ICP was done in Russia, at the Institute for Problems in Mechanics (IPM) with the series of Inductive Plasma Generators (IPG) [1, 2, 3, 4]. The IRS (Institut für Raumfahrtsysteme of Stuttgart University) also developed its IPG facilities around the end of the eighties [5], until the development of the IPG-6 in 2012 [6]. In France, the CORIA ICP torch is operational since 1995 [7, 8]. In 1997, the most powerful ICP device in the world, the Plasmatron, was commissioned at the von Karman Institute for Fluid Dynamics (VKI) in Belgium [9]. More recent plasma torches have been built in the US (*e.g.* Vermont [10], Austin [11] and the very recent Plasmatron X in Illinois [12]).

The difficulty of running an ICP facility and performing measurements in several locations led to the development of dedicated numerical solvers to better prepare the experiments. The first numerical model of an ICP was developed by Boulos [13] in 1976 using a finite difference (FD) method. Further simulations were performed by the group of Proulx for monoatomic and molecular gases [14]. Various numerical solvers of increasing complexity based upon the finite volume (FV) method have also been proposed. Vanden Abeele [15] studied the physics of ICP using a two-temperature model of the plasma torch in non-equilibrium. Then, Magin [16] developed an axisymmetric code for equilibrium cases for the complete problem (torch and test chamber). Finally, Lani [17, 18] developed the COOLFluiD solver. More recently, the Center for Hypersonics and Entry Systems Studies (CHESS) at the University of Illinois at Urbana-Champaign developed a 3D, unsteady code for ICP [19], opening the path to capture 3D ICP modes and instabilities.

The previously mentioned solvers present several drawbacks. First, they are based on FV or FD second order total variation diminishing schemes on structured grids, demanding a high-quality mesh and numerous elements in high gradient regions. Moreover, low-order FV methods are not well suited for capturing unsteady phenomena such as instabilities or turbulence. For this reason, a higher-order accurate discretization is developed based upon the family of discontinuous Galerkin (DG) methods. DG methods were first introduced in 1973 by Reed and Hill [20] in the framework of hyperbolic problems. During the 1990s, there was an intensive development of DG methods for convection-diffusion problems (see *e.g.* the work of Cockburn and Shu [21]). In 2002, Arnold and Brezzi [22] analyzed the DG methods applied to purely elliptic problems and showed how to improve the stability, adjoint consistency and the convergence rate of the method. Although they were never used for ICP, DG codes were used in the case of high-enthalpy flows (*e.g.* Shrooyen et al. [23]). DG method present several advantages. They result in stable and accurate high-order discretization of the convective and diffusive operators on unstructured meshes of almost arbitrary quality. They allow for straightforward imposition of the boundary conditions and are very flexible to parallelization and adaptivity. The computational complexity of the methods is higher than standard methods, but this is offset by the computational efficiency and the gain in required degrees of freedom. This is further improved in combination with mesh and order (h and p) adaptation for which the methods are particularly well suited.

In this work, we use a variant of the classic DG method, called the hybridized discontinuous Galerkin (HDG) method. HDG was introduced to reduce computational complexity, improving the efficiency. Initially developed by Cockburn [24] for elliptic problems, the main advantage of the method is its reduced number of globally coupled degrees of freedom (DOFs), obtained *via* static condensation using hybrid variables, leading to non-negligible reduction of the computational costs and memory storage compared

to DG as pointed out by Woopen [25]. The method was further developed for linear and nonlinear convection-diffusion problems by Nguyen et al. [26, 27, 28]. It was later applied to several flow configuration (*e.g.* see Fernandez [29] for turbulent applications or the more recent work of Modave [30] for Helmholtz equation). In this work, we use a HDG framework developed by Woopen, Balan and May [31].

A second drawback of the legacy ICP codes is their solution strategy. They solve the electric field and the Navier-Stokes equations separately in a staggered fashion, slowing down the convergence or leading to instabilities [32, 33]. We propose to solve the system in a monolithic manner. This implementation requires to develop a multi-domain solver for the electric field equations outside the torch and the complete ICP equations (electric field and Navier-Stokes equations inside the torch). Although multi-domain solvers have been developed for classic DG methods (see for instance [34, 35]), to our best knowledge, this is the first multi-domain monolithic solver developed using HDG.

This work is presented as follows. First, a description of the plasma model is given. Then the multi-domain HDG method is presented. Finally, the results are discussed: first, a convergence study of the ICP model is presented using a manufactured solution, then, a comparison with the COOLFluiD (FV) code is shown [18]. Finally a comparison with experimental data is presented.

2. Model for inductively coupled plasma

This section aims at describing the physics underlying an inductively coupled plasma flow. First, a brief review of the working principles of the facility is given. Then, the basic assumptions are listed. Finally, the set of equations to be solved numerically is exposed.

2.1. Basic operating principles of an ICP facility

An inductively coupled plasma facility can be schematically represented in Fig. 1. It consists of a torch surrounded by coils. A gas (such as air for earth or argon for basic research study), enters the torch *via* an annular injector, creating a stabilizing recirculation. A partially ionized plasma is created by the electromagnetic coupling between the fluid and the high-frequency current in the surrounding coil *via* Joule effect. In order to further stabilize the flow, a swirl component is sometimes added to the injector. The plasma is then ejected in the test chamber, where pressure probes, calorimeters, Pitot tubes and a sample holder of ablation material are placed.

The physics underlying ICP flows is complex, as it is governed by the coupling between the fluid and an electromagnetic field. High density plasma involves complex chemical interactions that must be treated to capture flow features accurately. The walls of the facility are cooled down to a few hundred Kelvins through a water-cooled cold-cage system while the temperature at the torch center reaches 11 000 K, creating steep temperature gradients. The wide range of temperatures gives rise to strong variations in the fluid transport properties, such as viscosity or thermal conductivity. The pressure in the torch is almost constant everywhere, and the flow is near incompressible ($Ma \simeq 0.01$) and laminar ($Re \simeq 100$). In the chamber, the flow remains laminar and subsonic. Kelvin-Helmholtz instabilities occur in the jet shear layer, and the pressure field can be slightly affected by the presence of a sample material or probe. Large temperature gradients appear in the vicinity of cold samples placed in the jet.

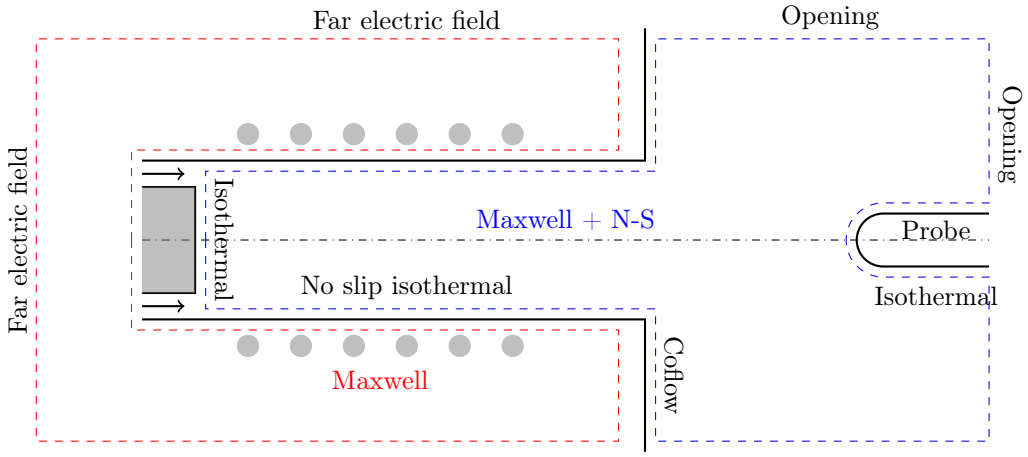

Figure 1: Schematic representation of an ICP. The torch is surrounded by coils (the grey disks) where an induction current flows. The injection system is annular in order to produce a recirculation close to the inlet, stabilizing the flow. The test material is placed in the chamber, after the torch exit. Conceptually, the Maxwell and Navier-Stokes equations are solved inside the torch (blue region), while only the Maxwell equations are solved outside (red region), making the ICP simulation a multi-domain problem. The boundary conditions have already been marked.

2.2. Thermodynamics

The plasma under consideration is a mixture at relatively high pressure ($p \simeq 5000 - 10\,000\,\mathrm{Pa}$), and at high induction current frequency ($f = 400\,\mathrm{kHz}$). It is assumed to be in local thermodynamic equilibrium (LTE) and elemental demixing is ignored. The LTE assumption is reasonable for the jet exhausting the torch but questionable for the plasma in the torch. Demixing effects remain significant even at high pressures [36] and should be considered in the future.

2.3. Plasma equations

The system of governing equations describing the flow of an inductively coupled plasma is composed of the Navier-Stokes and Maxwell equations. They are presented here, with the basic assumptions leading to the simplified ICP axisymmetric model. The interested reader can find a thorough derivation in [16].

Collision-dominated and thermal plasma The density of the plasma is relatively high. Consequently, the mean free path of the molecules is low and the plasma is dominated by molecular collision. The collisions are assumed to be sufficiently efficient so that all species have the same temperature. Also, the continuity hypothesis applies.

Quasi-neutrality The plasma characteristic length is assumed to be much larger than the Debye length, leading to a quasi-neutral plasma, where the electrostatic force produced by charged particles is driven by the collective behavior of the plasma and is responsible for diffusion phenomena.

No displacement current This assumption is valid if the oscillation frequency of the induction current is smaller than the plasma frequency, which represents the oscillation frequency of the free electrons about their equilibrium position. If the plasma frequency is very large, the electrons return rapidly to their equilibrium state and the electromagnetic waves produced by the excitation current are damped. On the other hand, it is assumed that the oscillation frequency is much larger than the plasma frequency. The electromagnetic and plasma waves always propagate in the torch and the displacement current can be neglected.

Ambipolar assumption It is commonly assumed that there is no diffusion current in the axisymmetric plane.

Splitting of the electric field The total electric ($\mathbf{E}$) field is split into an electrostatic ($\mathbf{E}_S$) and an induced ($\mathbf{E}_I$) parts

$$\mathbf{E} = \mathbf{E}_S + \mathbf{E}_I \tag{1}$$

Following the developments in [16], $\mathbf{E}_S$ is in the axisymmetric plane while $\mathbf{E}_I = E_I \mathbf{e}_\theta$ is assumed to be purely azimuthal. $\mathbf{E}_I$ is itself split into two contributions, one due to the coil $\mathbf{E}_C$ and one due to the plasma $\mathbf{E}_P$ electric field,

$$\mathbf{E}_I = \mathbf{E}_C + \mathbf{E}_P. \tag{2}$$

Axisymmetry Assuming axisymmetry excludes 3D plasma modes and coil-induced torch asymmetry [37]. Moreover, the coil is modeled as a series of infinitely thin parallel wires. The electric field from these loops is determined analytically [38, 39].

Weakly magnetized plasma The external magnetic field is too weak to affect plasma transport properties.

Non-radiative plasma No radiation is considered here, although radiation can have a huge impact on heat transfer caused by the medium itself at sufficiently high pressure [19]. Karl *et. al.* [40] have shown that a temperature difference of 1000 K is observed between radiative and non-radiative argon ICP simulations. These results are far from general, as the gas mixture and pressure in the facility play an important role. This should be investigated in future work, but requires a significant effort at both modelling and numerical levels.

No elemental demixing Elemental demixing is the separation of chemical elements by diffusion. This phenomenon is both present for equilibrium and non equilibrium flows [41]. It is ignored here.

Local thermodynamic equilibrium The ICP computations are assumed to be at local thermodynamic equilibrium (LTE). The thermodynamic properties of the gas are computed using a linear interpolation in a thermodynamic table of states built using the Mutation++ library [42]. This table primary serves to retrieve the fluid density, internal energy, viscosity, thermal conductivity and electric conductivity.

Steady-state We assume the flow to be at steady-state. In practice, ICP flows are unsteady due to the Kelvin-Helmholtz instabilities in the shear layer of the jet and

the fast temporal variation of the different fields introduced by the high oscillation frequency of the induction current. However, we disregard these effects, and average all variables over one oscillation period of the induction current. Then, in these time average equations, we find a steady solution ($\partial_t = 0$). However, we show the temporal derivative in our developments to keep the argument general.

Considering the previous hypotheses, the set of axisymmetric Navier-Stokes equations averaged over one oscillation period of the frequency is

$$\partial_t(r\mathbf{w}) + \partial_z\left(r\mathbf{F}_c^z - r\mathbf{F}_v^z\right) + \partial_r\left(r\mathbf{F}_c^r - r\mathbf{F}_v^r\right) = r\mathbf{S} \tag{3}$$

where the vector of conservative variables is $\mathbf{w} = \left(\rho \quad \rho v_z \quad \rho v_r \quad \rho v_\theta \quad \rho e + \rho\frac{||\mathbf{v}||^2}{2}\right)^T$, the total flux is split in a convective and diffusive parts $\mathbf{F} = \mathbf{F}_c - \mathbf{F}_d$, the convective flux vector is given by

$$\begin{aligned} F_c^z &= \left(\rho v_z \quad \rho v_z^2 + p \quad \rho v_z v_r \quad \rho v_z v_\theta \quad \rho v_z H\right)^T, \\ F_c^r &= \left(\rho v_r \quad \rho v_r v_z \quad \rho v_r^2 + p \quad \rho v_r v_\theta \quad \rho v_r H\right)^T, \end{aligned} \tag{4}$$

the diffusive flux vector is given by

$$\begin{aligned} F_d^z &= \left(0 \quad \tau_{zz} \quad \tau_{zr} \quad \tau_{z\theta} \quad \textstyle\sum_j \tau_{zj} v_j - q_z\right)^T, \\ F_d^r &= \left(0 \quad \tau_{rz} \quad \tau_{rr} \quad \tau_{r\theta} \quad \textstyle\sum_j \tau_{rj} v_j - q_r\right)^T, \end{aligned} \tag{5}$$

and the source terms are given by

$$S = \left(0 \quad F_z^L \quad \frac{p+\rho v_\theta^2 - \tau_{\theta\theta}}{r} + F_r^L \quad \frac{-\rho v_r v_\theta + \tau_{r\theta}}{r} \quad P_J\right)^T. \tag{6}$$

with ρ the density, $\mathbf{v} = (v_z \;\; v_r \;\; v_\theta)$ the velocity vector, p the static pressure, $H = \rho e + \rho\frac{||\mathbf{v}||^2}{2} + p$ the specific total enthalpy and $q = -k\nabla T$ the heat flux, with T the temperature of the fluid. The components of the symmetric viscous stress tensor in cylindrical coordinates are given by

$$\begin{aligned} \tau_{zz} &= 2\eta\left(\partial_z v_z - \frac{1}{3}\nabla\cdot\mathbf{v}\right) & \tau_{rr} &= 2\eta\left(\partial_r v_r - \frac{1}{3}\nabla\cdot\mathbf{v}\right) \\ \tau_{zr} &= \tau_{rz} = \eta\left(\partial_r v_z + \partial_z v_r\right) & \tau_{r\theta} &= \eta\left(\partial_r v_\theta - \frac{v_\theta}{r}\right) \\ \tau_{z\theta} &= \eta\partial_z v_\theta & \tau_{\theta\theta} &= 2\eta\left(\frac{v_r}{r} - \frac{1}{3}\nabla\cdot\mathbf{v}\right) \end{aligned} \tag{7}$$

where η is the fluid dynamic viscosity and $\nabla\cdot\mathbf{v} = \partial_z v_z + \partial_r v_r + \frac{v_r}{r}$ is the divergence of the velocity field. Finally, the effective Lorentz force $\mathbf{F}^L$ and the power dissipated by joule heating P^J are linked to the real and imaginary parts (resp. E_I^{Im}, E_I^{Re}) of the induced electric field E_I (see Eq. (2))

$$\begin{aligned} F_z^L &= \frac{\sigma_e}{4\pi f}\left[E_I^{Im}\partial_z E_I^{Re} - E_I^{Re}\partial_z E_I^{Im}\right], \\ F_r^L &= \frac{\sigma_e}{4\pi f}\left[E_I^{Im}\frac{1}{r}\partial_r(rE_I^{Re}) - E_I^{Re}\frac{1}{r}\partial_r(rE_I^{Im})\right], \\ P^J &= \frac{\sigma_e}{2}\left[(E_I^{Im})^2 + (E_I^{Re})^2\right] \end{aligned} \tag{8}$$

where σ_e is the electronic electric conductivity of the plasma and f is the frequency of the induction current. The electron electric conductivity σ_e is assumed to dominate the ionic electric conductivity and therefore is the only electric conductivity appearing in the equations. The transport properties at equilibrium are computed using Mutation++ [42].

The equation for the electric field generated by the plasma E_P in the azimuthal direction is given by [16]

$$\partial_z \left(r\partial_z E_P\right) + \partial_r \left(r\partial_r E_P\right) - \frac{E_P}{r} = 2i\pi f \mu_0 \sigma_e r (E_C + E_P) \tag{9}$$

where E_C is the electric field produced by the coil, i is the imaginary unit, f is the coil induction frequency and μ_0 is the vacuum magnetic permeability. In the following, Eq. (3) and (9) are solved using the HDG method. They are coupled through σ_e, which appears in the source term of both equations, and depends on temperature and pressure. The electric field produced by the coil can be computed analytically from the following equation

$$\partial_z(r\partial_z E_C) + \partial_r(r\partial_r E_C) - \frac{E_C}{r} = 2i\pi f \mu_0 I_C \sum_{j=1}^{n_r} \delta(\mathbf{x} - \mathbf{x}_j) \tag{10}$$

where I_C is the magnitude of the current flowing through the coil, and $\mathbf{x}_j$ is the position of coil j. The interested reader may refer to [38] for a complete derivation of E_C using Maxwell equations. The coil electric field E_C is given by

$$E_C = \sum_{j=1}^{n_r} i f \mu_0 I_C \sqrt{\frac{r_0}{r}} \left[2\frac{E_2(k_j)}{k_j} - E_1(k_j) \left(\frac{2}{k_j} - k_j \right) \right] \tag{11}$$

where $E_1(k)$ and $E_2(k)$ are respectively the complete elliptic integrals of the first and second kind

$$E_1(k) = \int_0^{\frac{\pi}{2}} \frac{1}{\sqrt{1 - k^2 \sin^2(\theta)}}\, d\theta, \quad E_2(k) = \int_0^{\frac{\pi}{2}} \sqrt{1 - k^2 \sin^2(\theta)}\, d\theta, \tag{12}$$

with k_j defined as

$$k_j = \frac{4 r r_0}{(z - z_j)^2 + (r + r_0)^2}. \tag{13}$$

r_0 is the coil radius and z_j is the axial position of turn j. In practice, the coil electric field is computed once and for all at the beginning of the ICP simulation, then stored and reused as much as needed. The complete elliptic integrals are computed using the corresponding C++ standard library functions.

2.4. Computational domain, boundary and initial conditions

The ICP configuration is a multi-domain problem as shown in Fig. 1. It contains two subdomains: the torch, filled with conductive plasma, where Maxwell and Navier-Stokes equations are solved, and the outer region, governed by Maxwell equations and filled with non-conducting air at room temperature. The computational domain is accompanied by a set of boundary and initial conditions listed below.

2.4.1. Boundary conditions

The boundary conditions displayed in Fig. 1 are listed here.

Vanishing far electric field At the boundary of the Maxwell subdomain, the electric field vanishes: $E_P = 0$.

Symmetry axis The centerline is an axis of symmetry. $\partial_r p = 0$, $\partial_r u_z = 0$, $u_r = 0$, $\partial_r T = 0$ and $E_P = 0$.

Openings The chamber is cut to reduce the computational costs. Openings are placed at the cut location (top and right end of the chamber domain). $p = p_0$

No-slip wall isothermal The wall below the annular injector and the torch upper wall are isothermal. $T = T_{wall}$ and $\mathbf{u} = \mathbf{0}$.

Inflow The inflow is annular, $u_z = U_{in}$, $u_r = 0$ and $T = T_{inlet}$

Stabilizing coflow A stabilizing coflow is blown from the chamber upper left wall. The purpose of this coflow is to remove the Kelvin-Helmholtz instabilities occurring in the shear layer of the jet in order to reach steady-state. This technique has been used in legacy codes [43, 16, 44]. Since the coflow is injected outside of the torch radius, we can expect it to have no significant impact inside the jet for steady-state computations. Nevertheless, when the coflow is sufficiently low, Kelvin-Helmholtz instabilities appear in the shear layer, requiring a time-accurate solver. We do not investigate the effect of the coflow, and leave it for future work. $T = T_{wall}$, $\mathbf{u} = u_{coflow}\mathbf{e}_z$

Maxwell + N-S and Maxwell interface At the interface between Maxwell and ICP subdomains, boundary conditions are applied on the hydrodynamic fields. However, the normal electric field diffusive flux is conserved across the interface.

$$\begin{aligned} \nabla E_P^{Re,NS} \cdot \mathbf{n}^{NS} &= \nabla E_P^{Re,MAX} \cdot \mathbf{n}^{MAX} \\ \nabla E_P^{Im,NS} \cdot \mathbf{n}^{NS} &= \nabla E_P^{Im,MAX} \cdot \mathbf{n}^{MAX} \end{aligned} \tag{14}$$

where E_p^{Re} and E_p^{Im} represent the real and imaginary parts of the electric field, the superscripts NS and MAX label the N-S + Maxwell and Maxwell domains respectively, and $\mathbf{n}$ is the outward pointing normal with respect to a given subdomain.

2.4.2. Initial conditions

The flow is initialized as follows:

Velocity field Uniform initial velocity $\mathbf{v} = U_{in}\mathbf{e}_z$.

Temperature field Considering z and r the radial and axial position respectively:

- If $z > z_3$, or $r > R_{out}$, $T(z,r) = T_{wall}$.
- Else if $z \in [z_1; z_2]$, $T(z,r) = T_{12}(r) = T_{initial} + \frac{r^2}{R_{in}^2}(T_{wall} - T_{initial})$
- Else if $z < z_1$, $T(z,r) = \frac{T_{wall} - T_{12}(r)}{z_1^2} z^2 - 2\frac{T_{wall} - T_{12}(r)}{z_1} z + T_{wall}$

- Else if $z \in [z_2, z_3]$: $T(z,r) = T_{12}(r) + \frac{(z-z_2)^2}{(z_3-z_2)^2}(T_{wall} - T_{12}(r))$

The choice of z_1, z_2 and z_3 should be such that the initial data match the boundary conditions.

Pressure and electric field The pressure and electric fields are initialized as $E_P = 0$ and $p = p_0$. Note that the electric field is initialized the same way in both subdomains.

3. Numerical solution of inductively coupled plasma

We now describe the numerical solution of the steady ICP problem using a hybridized discontinuous Galerkin (HDG) method extended to multi-domain configurations. The numerical solver employed and the solution strategies are also discussed.

3.1. Problem statement

Multi-domain problems can be modeled as a collection of non-overlapping subdomains governed by their own physics. Consider a given subdomain $\Omega^l \subset \mathbb{R}^D$ of dimension D with boundary $\partial\Omega^l$. A set of conservation equations, boundary and initial conditions are defined over Ω^l as

$$
\begin{aligned}
&\partial_t \mathbf{w}^l(\mathbf{u}) + \nabla \cdot \left(\mathbf{F}_c^l(\mathbf{u}) - \mathbf{F}_v^l(\mathbf{u}, \nabla\mathbf{u})\right) = \mathbf{S}^l(\mathbf{u}, \nabla\mathbf{u}), && \mathbf{x} \in \Omega^l, && t > 0 \\
&\mathbf{u}^l = \mathbf{u}_{bc}^l, && \mathbf{x} \in \partial\Omega_d^l, && t > 0 \\
&\mathbf{F}_v^l \cdot \mathbf{n} = \mathbf{F}_{v,n,bc}^l, && \mathbf{x} \in \partial\Omega_n^l, && t > 0 \\
&\mathcal{F}^{l,l'}(\mathbf{u}^l, \nabla\mathbf{u}^l, \mathbf{u}^{l'}, \nabla\mathbf{u}^{l'}) = 0, && \mathbf{x} \in \gamma^{l,l'}, && t > 0,\ l \neq l' \\
&\mathbf{u}^l(t=0) = \mathbf{U}^l, && \mathbf{x} \in \Omega^l
\end{aligned}
\tag{15}
$$

where $\mathbf{u}^l$ is the vector of unknowns and $\mathbf{w}^l$ is the set of conservative variables. $\mathbf{F}_c$ and $\mathbf{F}_v$ are the convective and diffusive physical flux functions respectively and $\mathbf{S}$ represents the source terms. $\partial\Omega_d \subset \partial\Omega$ and $\partial\Omega_n \subset \partial\Omega$ are the part of the frontier where Dirichlet and Neumann boundary conditions apply respectively. $\mathbf{u}_{bc}$ and $\mathbf{F}_{v,n,bc}$ are boundary conditions on the solution and on the diffusive flux normal to the boundary respectively. $\mathbf{U}$ represents an initial field function. $\gamma^{l,l'} = \partial\Omega^l \cap \partial\Omega^{l'}$ is the common frontier to the subdomains l and l'. Finally, compatibility and conservation conditions are applied at the interface between domain Ω^l and $\Omega^{l'}$. They are represented by the function $\mathcal{F}$.

We have illustrated Eq. (15) particularized to the ICP model in Fig. 2. We show the conservative $\mathbf{w}$ and unknown $\mathbf{u}$ vectors for each subdomain, and the conservativity condition $\mathcal{F}$ across their boundary. We also have listed in Table 1 the mapping of the symbols found in Eq. (15) and in the ICP problem. The boundary and initial conditions can be retrieved from Section 2.4. Note that, for the Navier-Stokes equations, we use the set of unknowns $\mathbf{u} = (p\ v_z\ v_r\ v_\theta\ T)$. This choice is mainly motivated by the use of an LTE table of state constructed using p and T. It is then easy to retrieve the usual conservative quantities $\mathbf{w} = (\rho\ \rho v_z\ \rho v_r\ \rho v_\theta\ e + \rho\frac{||\mathbf{v}||^2}{2})$ using the LTE table. Note also that, outside of the torch, the air is considered to be insulating, meaning that the right hand side of Eq. (9) vanishes in this region. Finally, E_C and E_P are split into a real and imaginary parts, and so is Eq. (9).

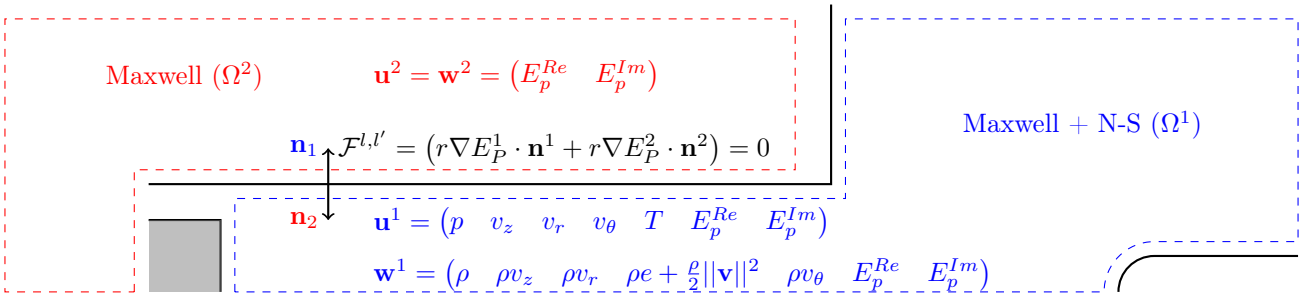

Figure 2: Schematic representation of an ICP as a multi-domain problem. Only half of the facility is represented. The two domains are Ω^1, the Navier-Stokes + Maxwell subdomain, and Ω^2 the Maxwell subdomain. The conservative variables $\mathbf{w}^l$ and $\mathbf{u}^l$ have been shown for each domain, with ρ the density of the fluid, v_z and v_r the radial and axial velocity components, T the temperature, e the internal energy, p the pressure, $E_P = E_P^{Re} + iE_P^{Im}$ the plasma electric field, with E_P^{Re} and E_P^{Im} its real and imaginary parts. The operator $\mathcal{F}$ has also been displayed, representing the conservation of the electric field diffusive flux across subdomains.

Eq. (15)	**NS** + **Maxwell** (Eq. (3) + Eq. (9))	**Maxwell** (Eq. (9))
$\mathbf{u}^l$	$\begin{pmatrix} p & v_z & v_r & v_\theta & T & E_P^{Re} & E_P^{Im} \end{pmatrix}^T$	$\begin{pmatrix} E_P^{Re} & E_P^{Im} \end{pmatrix}^T$
$\mathbf{w}^l$	$\begin{pmatrix} \rho & \rho v_z & \rho v_r & \rho v_\theta & \rho e + \rho \frac{\|\|\mathbf{v}\|\|^2}{2} & E_P^{Re} & E_P^{Im} \end{pmatrix}^T$	$\begin{pmatrix} E_P^{Re} & E_P^{Im} \end{pmatrix}^T$
$\mathbf{F}_c^l$	$\begin{pmatrix} r\mathbf{F}_c & 0 & 0 \end{pmatrix}^T$, $\mathbf{F}_c$ is given in Eq. (4)	/
$\mathbf{F}_v^l$	$r \begin{pmatrix} \mathbf{F}_v & \nabla E_P^{Re} & \nabla E_P^{Im} \end{pmatrix}^T$, $\mathbf{F}_v$ is given in Eq. (5)	$r \begin{pmatrix} \nabla E_P^{Re} & \nabla E_P^{Im} \end{pmatrix}^T$
$\mathbf{S}^l$	$\begin{pmatrix} r\mathbf{S} \\ 2\pi f \mu_0 \sigma_e r (E_C^{Im} + E_P^{Im}) - \frac{E_P^{Re}}{r} \\ -2\pi f \mu_0 \sigma_e r (E_C^{Re} + E_P^{Re}) - \frac{E_P^{Im}}{r} \end{pmatrix}$, $\mathbf{S}$ is given in Eq. (6)	$\begin{pmatrix} -\frac{E_P^{Re}}{r} \\ -\frac{E_P^{Im}}{r} \end{pmatrix}$
$\mathcal{F}^{l,l'}$	$r \begin{pmatrix} \nabla E_P^{Re,NS} \cdot \mathbf{n}^{NS} + \nabla E_P^{Re,MAX} \cdot \mathbf{n}^{MAX} \\ \nabla E_P^{Im,NS} \cdot \mathbf{n}^{NS} + \nabla E_P^{Im,MAX} \cdot \mathbf{n}^{MAX} \end{pmatrix}$	
$\mathbf{u}_{bc}^l$	$\mathbf{u}$ evaluated using the boundary values in Section 2.4.1	
$\mathbf{F}_{v,n,bc}^l$	$\mathbf{F}_v \cdot \mathbf{n}$, evaluated using $\mathbf{u}_{bc}$ and the gradient boundary values in Section 2.4.1	
$\mathbf{U}^l$	$\mathbf{u}$, evaluated using the initial values as described in Section 2.4.2	

Table 1: Mapping table between the notations of Eq. (15) and the notations of the ICP problem composed of the N-S + Maxwell subdomain (Eq. (3) + Eq. (9)) and the Maxwell subdomain (Eq. (9)). ρ is the density of the fluid, v_z, v_r and v_θ are the axial, radial and azimuthal velocity components respectively, T is the temperature, e is the internal energy, p is the pressure, E_P^{Re} and E_P^{Im} are the real and imaginary parts of the electric field respectively and r is the radial position. $\mathbf{n}$ represents the outward pointing normal to the boundary of a specific subdomain. The superscripts NS and MAX label the Maxwell + Navier-Stokes and the Maxwell domain respectively.

3.2. Hybridized Discontinuous Galerkin method

We describe the hybridized discontinuous Galerkin (HDG) method. The developments follow closely [26, 28, 45, 31]. We first give the HDG spatial discretization and functional spaces. Then, we discuss the discrete problem. We also present the numerical fluxes and the compatibility and conservativity conditions between subdomains for the case of ICP simulations.

3.2.1. Spatial discretization

Let us consider a domain Ω composed of N_d non-overlapping subdomains Ω_l:

$$\Omega = \bigcup_{l=1}^{N_d} \Omega^l. \tag{16}$$

Each subdomain Ω^l is divided in a collection $\mathcal{T}^l$ of N_e^l non-overlapping elements labeled by K_i. The tesselation $\mathcal{T}$ of the complete domain Ω is defined as $\mathcal{T} = \bigcup_{l=1}^{N_d} \mathcal{T}^l$, with boundary $\partial\mathcal{T}$. The subdomain mesh skeleton Γ^l is defined as

$$\Gamma^l = \{e : e = K_i \cap K_j; \forall K_i, K_j \in \mathcal{T}^l,\ K_i \neq K_j\}. \tag{17}$$

We also define the set of traces on the interface between subdomains $\Gamma^{l,l'}$ as

$$\Gamma^{l,l'} = \{e : e = K \cap K'; K \in \mathcal{T}^l, K' \in \mathcal{T}^{l'},\ l \neq l'\} \tag{18}$$

In the following, we define Γ as the set containing all traces Γ^l and $\Gamma^{l,l'}$, and by $\bar{\Gamma}$ the set containing all the traces located at the interface between subdomains.

3.2.2. Functional spaces

The purpose of HDG is to find an approximation to the solution $\mathbf{u}$ of Eq. (15) and its gradient $\mathbf{q} = \nabla\mathbf{u}$ on finite dimensional functional spaces. To do so, it also uses a set of hybrid degrees of freedom on the mesh skeleton, noted $\boldsymbol{\lambda}$ in the following. They represent the solution on the element interface. Considering the sets $\mathcal{P}^p(K)$ of polynomial of degree at most p over the set K, we define those sets W_h, V_h and M_h as:

$$W_h = \left\{w \in L^2(\Omega) : w|_K \in \mathcal{P}^p(K), \forall K \in \mathcal{T}\right\} \tag{19}$$

$$V_h = \left\{\mathbf{v} \in L^2(\Omega) : \mathbf{v}|_K \in (\mathcal{P}^p(K))^d, \forall K \in \mathcal{T}\right\} \tag{20}$$

$$M_h = \left\{\mu \in L^2(\Gamma) : \mu|_e \in \mathcal{P}^p(e), \forall e \in \Gamma\right\} \tag{21}$$

$$\tag{22}$$

with d the spatial dimensions of the problem. In this work, Dubiner's polynomial basis with compact support on the element is used for all spaces [46]. Consequently, the solution $\mathbf{u}_h$, solution gradient $\mathbf{q}_h$ and the hybrid variables λ_h on facet e are given by

$$\mathbf{u}_h = \sum_{K\in\mathcal{T}} \sum_{i=1}^{p} \mathbf{u}_{K,i}\varphi_{K,i} \quad \mathbf{q}_h = \sum_{K\in\mathcal{T}} \sum_{i=1}^{p} \mathbf{q}_{K,i}\boldsymbol{\tau}_{K,i} \quad \boldsymbol{\lambda}_h = \sum_{e\in\Gamma} \sum_{i=1}^{p} \boldsymbol{\lambda}_{e,i}\mu_{e,i}. \tag{23}$$

with $(\varphi_{K,i}, \boldsymbol{\tau}_{K,i}, \mu_{e,i}) \in W_h \times V_h \times M_h$ the Dubiner's basis functions with compact support on element $K \in \mathcal{T}$ and $e \in \Gamma$, $i \in \{1, 2, ..., p\}$.

3.2.3. Notations

We present here some of the operators and symbols. The jump operator is defined at the interface between elements as

$$[[\mathbf{u}]] = \mathbf{u}_+ \cdot \mathbf{n}_+ + \mathbf{u}_- \cdot \mathbf{n}_-, \tag{24}$$

where the $+$ and $-$ label the two elements sharing the edge over which the jump is computed, $\mathbf{n}$ represents the outward pointing normal to an element. We also define the following integration operators:

$$(a,b)_K = \int_K ab \; dV \quad \langle a,b\rangle_{\partial K} = \int_{\partial K} ab \; dS \tag{25}$$

3.2.4. Discrete problem

The HDG method adapted to a multi-domain problem consists in, for each subdomain $\Omega^l \in \Omega$ tesselated using the set $\mathcal{T}^l \in \mathcal{T}$, finding an approximation of the solution of the model problem Eq. (15) by solving the following problem for $(\mathbf{u}_h, \mathbf{q}_h, \boldsymbol{\lambda}_h) \in W_h \times V_h \times M_h$ and for any test function $(v, \boldsymbol{\tau}, \pi) \in W_h \times V_h \times M_h$:

$$\begin{aligned}
&\left(\partial_t \mathbf{w}_h^l - \mathbf{S}_h^l, v\right)_{\mathcal{T}^l} - \left(\mathbf{F}_{h,c}^l - \mathbf{F}_{h,v}^l, \nabla v\right)_{\mathcal{T}^l} + \sum_{K\in\mathcal{T}} \left\langle \boldsymbol{\mathcal{H}}^l, v \right\rangle_{\partial K} = 0 \\
&\left(\mathbf{q}_h^l, \boldsymbol{\tau}\right)_{\mathcal{T}^l} - \left(\mathbf{u}_h^l, \nabla\boldsymbol{\tau}\right)_{\mathcal{T}} + \sum_{K\in\mathcal{T}^l} \left\langle \boldsymbol{\lambda}_h^l, \boldsymbol{\tau}\cdot\mathbf{n} \right\rangle_{\partial K\setminus\partial\Omega^l} + \left\langle \mathbf{u}_{bc}^l, \boldsymbol{\tau}\cdot\mathbf{n}\right\rangle_{\partial\Omega^l} = 0 \\
&\left\langle [[\boldsymbol{\mathcal{H}}^l]], \pi \right\rangle_{\Gamma^l} + \sum_{\substack{l'=1 \\ l'\neq l}}^{N_d} \langle \tilde{\mathcal{F}}^{l,l'}, \pi\rangle_{\Gamma^{l,l'}} = 0
\end{aligned} \tag{26}$$

where the subscript h means that a quantity is evaluated using $\mathbf{u}_h$, $\mathbf{q}_h$ and $\boldsymbol{\lambda}_h$, the superscript l denotes the domain and N_d is the number of subdomains inside Ω. $\boldsymbol{\mathcal{H}}$ is the numerical flux function, *i.e.* an approximate consistent evaluation of the convective and diffusive physical fluxes at the interface used to stabilize the method. Eq. (26) is very similar to classic HDG. However, the third equation contains an additional term, which is the core of the multi-domain method presented in this work

$$\sum_{\substack{l'=1 \\ l'\neq l}}^{N_d} \langle \tilde{\mathcal{F}}^{l,l'}, \mu\rangle_{\Gamma^{l,l'}}. \tag{27}$$

The operator $\tilde{\mathcal{F}}$ is responsible for the exchange of information between subdomains Ω^l and $\Omega^{l'}$. In general, $\tilde{\mathcal{F}}$ is an approximation to $\mathcal{F}$, the actual compatibility or conservativity condition existing between the subdomains. Both the numerical flux functions $\boldsymbol{\mathcal{H}}$ and $\tilde{\mathcal{F}}$ are discussed more thoroughly in the following.

Because the sets W_h, V_h and M_h are finite dimensional, as long as Eq. (26) is verified for the basis functions, it is verified for all functions $(v, \boldsymbol{\tau}, \pi) \in V_h \times W_h \times M_h$. In DG methods, we use basis functions with compact support on the elements. Due to their

compact domain, Eq. (26) becomes, for all $K \in \mathcal{T}$, $e \in \Gamma$ and $i \in \{1, 2, ..., p\}$

$$\begin{aligned}
&\left(\partial_t \mathbf{w}_h^K - \mathbf{S}_h^K, \varphi_{K,i}\right)_K - \left(\mathbf{F}_{h,c}^K - \mathbf{F}_{h,v}^K, \nabla\varphi_{K,i}\right)_K + \left\langle \boldsymbol{\mathcal{H}}^K, \varphi_{K,i} \right\rangle_{\partial K} = 0 \\
&\left(\mathbf{q}_h^K, \boldsymbol{\tau}_{K,i}\right)_K - \left(\mathbf{u}_h^K, \nabla\boldsymbol{\tau}_{K',i}\right)_K + \left\langle \boldsymbol{\lambda}_h^{\partial K}, \boldsymbol{\tau}_{K,i} \cdot \mathbf{n} \right\rangle_{\partial K_0} + \langle \mathbf{u}_{bc}, \boldsymbol{\tau}_{K,i} \cdot \mathbf{n} \rangle_{\partial K_{bc}} = 0 \\
&\langle [[\boldsymbol{\mathcal{H}}]], \mu_{e,i} \rangle_{e \setminus \bar{\Gamma}} + \langle \tilde{\mathcal{F}}^e, \mu_{e,i} \rangle_{e \cap \bar{\Gamma}} = 0
\end{aligned} \tag{28}$$

where the index K and e denote the restriction to element $K \in \mathcal{T}$ and $e \in \Gamma$ respectively. Note that the mapping given in Table 1 apply to Eq. (28). The frontier of each element is $\partial K = \partial K_0 \bigcup \partial K_{bc}$, where the boundary condition apply on ∂K_{bc} and the part of the element frontier connected to another element is ∂K_0.

3.2.5. Numerical fluxes

The HDG method depends on the numerical flux $\boldsymbol{\mathcal{H}}$. This flux can be written as $\boldsymbol{\mathcal{H}} = \boldsymbol{\mathcal{H}}_c - \boldsymbol{\mathcal{H}}_v$, where $\boldsymbol{\mathcal{H}}_c$ and $\boldsymbol{\mathcal{H}}_v$ are the convective and diffusive contributions. It plays an important role in the stability, convergence and in the imposition of boundary conditions of the method. We present here numerical fluxes specifically applied to the problem of ICP flows.

Convective numerical flux. ICP flows are incompressible, since $Ma \simeq 0.01$. In these regimes, pressure cannot be updated easily [47], leading to a loss of accuracy and unstable solvers. We use here a convective numerical flux specifically designed for low-Mach regimes, belonging to the the Advection Upstream Splitting Method (AUSM) family. The AUSM scheme was first presented in the seminal work of Liou [48, 49, 50]. It is based on the splitting of the convective flux into a pressure part and an upwind convective part. The resulting flux is designed to be central in the low-mach number limit and upwind in the supersonic case. A simplified version of AUSM for $Ma \to 0$ has already been employed by Magin [16] in FV, where a pressure diffusion term is added to the momentum transport flux. We adapted this simplified version to the HDG method for the axisymmetric version of Navier-Stokes equation:

$$\boldsymbol{\mathcal{H}}_c^n(\lambda, u) = \frac{r}{2}(\dot{m} + \dot{m}_p)(\Psi_\lambda + \Psi_U) - \frac{r}{2}|\dot{m}|(\Psi_\lambda - \Psi_U) + r\mathbf{P}, \tag{29}$$

where

$$\boldsymbol{\Psi} = \begin{pmatrix} 1 & v^\perp & v^\parallel & v_\theta & e + \frac{1}{2}||\mathbf{v}||^2 + \frac{p}{\rho} \end{pmatrix}^T, \tag{30}$$

with the $\parallel$ and $\perp$ superscript respectively denoting the perpendicular and parallel components of a vector with respect to the normal direction to the facet, p is the pressure, ρ is the density, e is the internal energy and $\mathbf{v}$ is the velocity vector. The subscripts U and λ represent respectively the values in the element and on the facet, $\dot{m} = \frac{1}{4}\left(\rho_\lambda + \rho_U\right)\left(v_\lambda^\perp + v_U^\perp\right)$ is the average mass flow rate, while $m_p = \frac{p_U - p_\lambda}{V_p}$ is the pressure diffusion factor, with V_p a preconditioning velocity, chosen as a characteristic velocity of the flow (in our case, the inlet velocity). Finally, the pressure flux is defined as $\mathbf{P} = \begin{pmatrix} 0 & \frac{p_\lambda + p_U}{2} & 0 & 0 \end{pmatrix}^T$. In order to express the convective numerical flux in the axisymmetric frame of reference,

one must multiply it by a rotation matrix:

$$\boldsymbol{\mathcal{H}}_c = \begin{pmatrix} 1 & 0 & 0 & 0 & 0 \\ 0 & n_z & -n_r & 0 & 0 \\ 0 & n_r & n_z & 0 & 0 \\ 0 & 0 & 0 & 1 & 0 \\ 0 & 0 & 0 & 0 & 1 \end{pmatrix} \boldsymbol{\mathcal{H}}_c^n, \tag{31}$$

with n_z and n_r the components of the normal vector to the facet.

Diffusive numerical flux. The diffusive numerical flux is discretized as follows

$$\boldsymbol{\mathcal{H}}_v^l(u, \lambda, q) = \frac{1}{2}\left(\mathbf{F}_v^l(\boldsymbol{\lambda}, \mathbf{q}) + \mathbf{F}_v^l(\mathbf{u}, \mathbf{q})\right) \cdot \mathbf{n} + \gamma(h)(\boldsymbol{\lambda} - \mathbf{u}) \tag{32}$$

where the definition of $\mathbf{F}_v^l$ for both subdomains can be retrieved from Table 1. The penalization parameter γ depends on a local characteristic mesh size. γ has been widely studied for DG methods (see for instance [51, 52, 53]). Based on these results, we suggest a form of γ very close to the one proposed by Hillewaert [51]:

$$\gamma = C \max_{K \ni f} \left(\frac{1}{2\mathcal{V}} \sum_{f \in K} \mathcal{A} \right) \tag{33}$$

with f denoting the facet under consideration, K being an element sharing the facet, C a multiplicative constant proportional to the physical diffusion processes (such as viscosity, heat conductivity), $\mathcal{A}$ is the area of the facet (length in 2D), $\mathcal{V}$ is the volume of the element (surface in 2D).

Imposing boundary conditions. The boundary conditions are weakly imposed through the numerical flux $\boldsymbol{\mathcal{H}}(\mathbf{u}, \mathbf{q}, \mathbf{u}_{bc}, \mathbf{q}_{bc})$, where $\mathbf{u}_{bc}$ and $\mathbf{q}_{bc}$ are respectively the boundary condition and boundary condition gradient given in Section 2.4.1. If no BC is applied, the value is copied from inside the domain ($\mathbf{u}_{bc} = \mathbf{u}$ and/or $\mathbf{q}_{bc} = \mathbf{q}$).

3.2.6. Compatibility and conservativity conditions between subdomains

The compatibility and conservativity conditions between neighbouring subdomains are treated in the third equation of Eq. (28). This equation contains an additional term compared to single domain HDG. It takes into account the discretization of the $\mathcal{F}$ operator, labelled here $\tilde{\mathcal{F}}$.

If $\mathcal{F}$ represents the conservativity of a flux across the interface, then the discretization $\tilde{\mathcal{F}}$ is the conservation of the associated numerical flux across that interface. In the case of ICP, the conservation of the normal diffusive electric flux gives:

$$\tilde{\mathcal{F}} = \begin{pmatrix} \mathcal{H}_{v,E_p^{Re}}^{NS} + \mathcal{H}_{v,E_p^{Re}}^{MAX} \\ \\ \mathcal{H}_{v,E_p^{Im}}^{NS} + \mathcal{H}_{v,E_p^{Im}}^{MAX} \end{pmatrix} \tag{34}$$

where $\mathcal{H}_{v,E_p^{Re}}$ and $\mathcal{H}_{v,E_p^{Im}}$ represents the diffusive numerical flux of the real and imaginary electric field respectively and the superscripts MAX and NS represent the Maxwell

and the Maxwell + Navier-Stokes subdomains respectively. The complete expression of $\mathcal{H}_{v,E_p^{Re}}$ and $\mathcal{H}_{v,E_p^{Im}}$ can be found in Eq. (32).

In other physical problem, $\mathcal{F}$ may represent a compatibility condition, such as a jump or continuity of a variable across the interface. Since this is not the case here, we do not develop this topic further. The interested reader may refer to [54] for an example of application of a compatibility condition.

3.3. Solution strategy

Eq. (28) is solved using Newton's method and eliminating the local variables in order to obtain a global system for the hybrid unknowns. The resulting hybrid solution $\boldsymbol{\lambda}$ is used to reconstruct the element-wise solutions $(\mathbf{u}, \mathbf{q})$ using direct inversion of small local matrices. We describe here the strategy for reaching steady-state. Unsteady computations are left for future work.

3.3.1. Damped inexact Newton-Raphson method

Since we are interested in steady-state computations, a damped inexact Newton iteration is used in this work. It consists in adding a fictitious temporal term to the steady-state form of the equations ($\partial_t = 0$). The role of this pseudo-temporal term is to ease the convergence towards the steady-state, especially when the initial data are far from the steady solution. When the CFL is sufficiently large, this term becomes negligible, and the steady-state solution is retrieved. This is translated in Eq. (28) by replacing the time derivative of the conservative variables $\mathbf{w}^l$ associated to the subdomain l by a finite difference approximation:

$$\partial_t \mathbf{w}^K(\mathbf{u}_K) \simeq \frac{\mathbf{w}^K(\mathbf{u}_K^k) - \mathbf{w}^K(\mathbf{u}_K^{k-1})}{\tau_K} \tag{35}$$

where k denotes the current Newton iteration. $\tau_K = CFL \times h_K/v_K$ is a local time step associated to element K. It is defined *via* a global Courant-Friederichs-Lewy number, the characteristic size h_K and speed v_K of each element. In this work, $\frac{h_K}{v_K} = \frac{V_K}{\int_{\partial K} \lambda_{max} dS}$, where λ_{max} is the maximal eigenvalue of the hyperbolic operator and V_K is the volume (or area in 2D) of the element K. The choice of the CFL is based on the evolution of L_2 norm of the residual $\mathcal{R}$ of the system. It is given by

$$CFL^n = \min\left(CFL_0 \left(\frac{||\mathcal{R}||_2^0}{||\mathcal{R}||_2^n}\right)^{\alpha}, CFL_{max}\right) \tag{36}$$

where the index 0 denotes the initial value of a quantity, and CFL_{max} is a CFL upper bound. α is an exponent factor governing the evolution of the CFL.

3.3.2. Global and local problems

Eq. (28) can be cast in a generic form using a nonlinear operator $\mathcal{N}$

$$\mathcal{N}_h(\mathbf{x}_h; \mathbf{y}_i) = 0 \tag{37}$$

where $\mathbf{x}_h = (\boldsymbol{\lambda}_h^n, \mathbf{u}_h^n, \mathbf{q}_h^n)$ is the vector of unknowns and $\mathbf{y}_i = (\mu_i, \varphi_i, \boldsymbol{\tau}_i)$ is the vector containing the basis functions of the approximate functional spaces. Eq. (37) can be linearized and solved using the Newton-Raphson method

$$\mathcal{N}_h'(\mathbf{x}_h^k; \mathbf{y}_i)\delta\mathbf{x}_h^k = -\mathcal{N}_h(\mathbf{x}_h^k; \mathbf{y}_i). \tag{38}$$

The iterative procedure is started from an initial guess $\mathbf{x}_h^0$. From there, the solutions $\mathbf{x}^{k+1}$ are computed by solving successively Eq. (38) using $\mathbf{x}^k$ as an initial guess: $\mathbf{x}^{k+1} = \mathbf{x}^k + \delta\mathbf{x}^k$. The algorithm is stopped when the norm of the residual is sufficiently low.

Following this procedure, Eq. (38) is written for HDG as:

$$\underbrace{\begin{pmatrix} A & B & R \\ C & D & S \\ L & M & N \end{pmatrix}}_{\mathcal{N}_h'(\mathbf{x}_h^k;\mathbf{y}_i)} \overbrace{\begin{pmatrix} \delta Q \\ \delta U \\ \delta\Lambda \end{pmatrix}}^{\delta\mathbf{x}_h^k} = \underbrace{\begin{pmatrix} F \\ G \\ H \end{pmatrix}}_{-\mathcal{N}_h(\mathbf{x}_h^k;\mathbf{y}_i)}, \tag{39}$$

Eq. (39) can be rewritten in two sets of equations:

$$\Sigma \begin{pmatrix} \delta Q \\ \delta U \end{pmatrix} = \begin{pmatrix} F \\ G \end{pmatrix} - \begin{pmatrix} R \\ S \end{pmatrix} \delta\Lambda, \text{ with } \Sigma = \begin{pmatrix} A & B \\ C & D \end{pmatrix} \tag{40}$$

and

$$\begin{pmatrix} L & M \end{pmatrix} \begin{pmatrix} \delta Q \\ \delta U \end{pmatrix} + N\delta\Lambda = H \tag{41}$$

Eq. (40) is called the local system, because Σ is block diagonal, with each block associated to an element. Therefore, it is possible to eliminate the local variables from Eq. (41) by directly inverting Σ, leading to a global system for the hybrid unknowns:

$$\left(N - \begin{pmatrix} L & M \end{pmatrix} \Sigma^{-1} \begin{pmatrix} R \\ S \end{pmatrix} \right) \delta\Lambda = H - \begin{pmatrix} L & M \end{pmatrix} \Sigma^{-1} \begin{pmatrix} F \\ G \end{pmatrix} \tag{42}$$

Then, the linear system given in Eq. (42) is solved with the PETSc library [55]. A GMRES method is employed with at most 50 basis vectors. An ILU preconditioner with 4 levels of filling is used.

3.3.3. Newton-Raphson method and constant power

In ICP facilities, part of the power supplied to the generator is dissipated in the form of Joule heating in the plasma. Let us call this part P_{target}. There is no straightforward relation linking the current I_C to be imposed in the coil and P_{target}. This is also true for ICP simulations. Additionally, if I_C does not maintain the desired power during the computations, the torch is quenched [13]. To avoid this, the current is updated at each Newton iteration, allowing the power to converge towards P_{target}. This method, inspired from legacy ICP solvers [43, 15], is described in the following.

Let us define γ, the ratio of the desired power P_{target} and the power actually dissipated in the facility P_{tot}:

$$\gamma = \frac{P_{target}}{P_{tot}}, \quad P_{tot} = \int_{NS} \frac{\sigma}{2} ||E_C + E_P||^2 dV \tag{43}$$

Consequently, the target power is given by

$$P_{target} = \gamma P_{tot} = \int_{NS} \gamma \frac{\sigma}{2} ||E_C + E_P||^2 dV \tag{44}$$

Reaching the target power is thus equivalent to multiply E_P and I_C (or equivalently E_C, see Eq. (11)) by $\sqrt{\gamma}$. If we neglect the coupling between Maxwell and Navier-Stokes equations, Eq. (9) is linear and $\sqrt{\gamma}E_P$ and $\sqrt{\gamma}E_C$ is also a solution. Then, each Newton iteration occurs as follows:

1. The ICP problem is solved for a given value of I_C for one Newton iteration.
2. At the end of the Newton iteration, γ is computed using Eq. (43).
3. I_C and E_P are multiplied by $\sqrt{\gamma}$, and used in the next Newton iteration. Note that, by linearity, the new E_P associated with the new source term E_C is also a solution of Eq. (9).

In practice, we use an equivalent method to avoid updating the electric field and current at each iteration. We solve Eq. (9) with $I_C = 1\,\mathrm{A}$ for each Newton iteration. The power factor γ is used as a multiplicative constant in the effective Lorentz force and Joule heating source terms (Eq. (3)), and is the only parameter to be updated. The actual electric fields and current can be retrieved by multiplying E_C, E_P and I_C by $\sqrt{\gamma}$ at the end of the simulation. The computation of P_{tot} and γ occurs after setting the initial data and at the end of each Newton iteration (see Algorithm 1).

3.3.4. Solution procedure

The solution procedure employed with the HDG code (Fig. 3) is quite different from the previous solvers such as COOLFluiD (Fig. 4). In the HDG code, the system of equation (ICP + Maxwell) is solved in a fully coupled manner. On the other hand, the FV solver decouples the solutions of Maxwell and Navier-Stokes equations, solving them separately by assuming that all hydrodynamic quantities are frozen while solving the electric field, and *vice-versa*. While the latter procedure is easier to implement, it takes more Newton iterations to converge (on the order of thousand of iterations) than the monolithic solver (on the order of 10-100 iterations). The monolithic solution procedure is presented in Algorithm. 1.

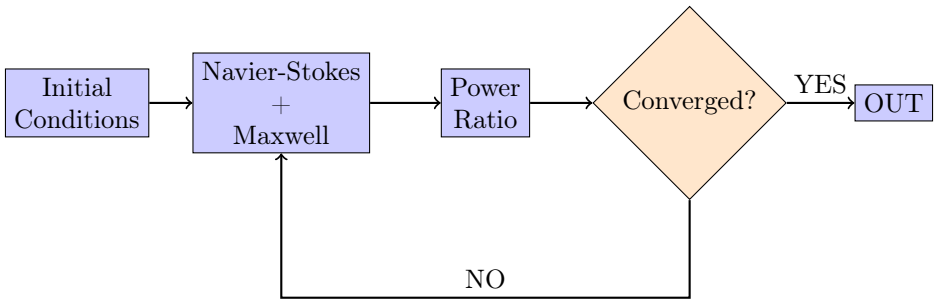

Figure 3: Diagram of the solution procedure of ICP simulations using the HDG method. The Navier-Stokes and Maxwell equations are solved in a fully coupled manner.

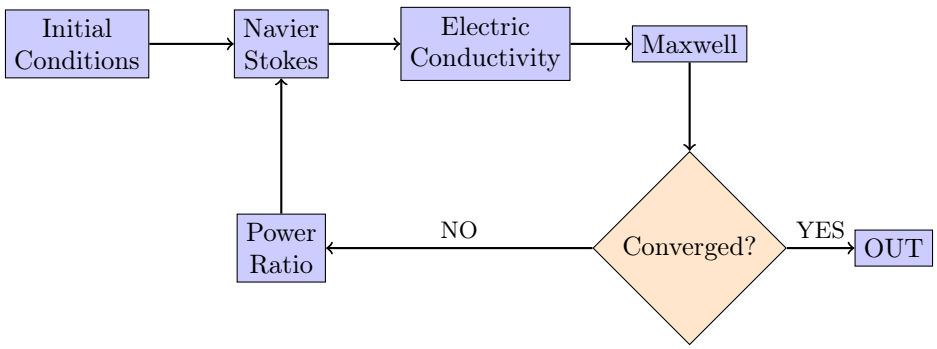

Figure 4: Diagram of the solution procedure of ICP simulations using the COOLFluiD FV solver. The system is solved in a decoupled manner: one system is frozen while the other is solved. The process is repeated until convergence occurs. This diagram was inspired by [56]

Algorithm 1 Solution procedure for multi-domain HDG

Set all simulation parameters
Initialize λ_h, w_h, q_h;
Compute P_{tot} and γ using Eq. (43);
while $||Residual||_2 >$ Tolerance **do**
  for l = 1, ..., N_d **do**
    for i = 1,..., N_e **do**
      Assemble local system (Eq. (40)) of subdomain l;
      - The Lorentz and Joule source terms of N-S (Eq. (3)) are multiplied by γ.
      - The electric field equation (Eq. (9)) is always solved using $I_c = 1$.
      Solve local system of subdomain l;
      Store local solution of subdomain l;
      Assemble global system (Eq. (42));
    end for
  end for
  Solve global system;
  Update λ_h, w_h, q_h;
  Compute P_{tot} and γ using Eq. (43);
end while
Multiply I_C (or E_C) and E_P by $\sqrt{\gamma}$ to obtain the actual value of the electric fields and current;

4. Results

We first present a convergence study of the multi-domain ICP solver using a manufactured solution. The goal is to prove that the order of convergence is retrieved. Then, the results of the HDG code are compared to the results obtained from the COOLFluiD simulations on an ICP case with a probe. COOLFluiD is a finite volume code [18] able to perform ICP computations using a second order TVD flux reconstruction. It is currently used by VKI experimentalists in order to assist them during ICP experimental campaigns. Finally, the results of the HDG code are validated using radial temperature profiles measured experimentally in the Plasmatron facility.

4.1. Convergence study on a manufactured solution

While studying the convergence of DG-like methods towards a reference solution, it is important to use solutions that cannot be exactly represented by the basis of the functional space employed. Otherwise, the solution is going to be exactly captured, irrespectively of the mesh. Due to the complexity of finding such reference solutions, they are manufactured, meaning that the source terms of Eq. (3) and Eq. (9) are modified in order to match a user defined solution.

4.1.1. Manufacturing a solution for ICP

The manufactured solution for ICP equation is tested on an axisymmetric domain delimited by two concentric cylinders of radii $R_1 = 0.486\,\mathrm{m}$ and $R_2 = 0.972\,\mathrm{m}$ respectively and length $L = 0.486\,\mathrm{m}$. The region inside the first cylinder is governed by the full ICP equations (Maxwell and Navier-Stokes), while the other region delimited by the radii is ruled by Maxwell equations. The solutions chosen for the various fields are:

$$\begin{aligned} p &= \Delta p_0 f(z,r) + p_0 \quad & T &= T_{min} + (T_{max} - T_{min})\, f(z,r) \\ u &= u_0 f(z,r) & E_p &= E_0 \sin\left(\frac{\pi r^2 z}{L R_1}\right)(1-i) \\ v &= v_0 f(z,r) \end{aligned} \tag{45}$$

with $p_0 = 5000\,\mathrm{Pa}$, $\Delta p = -10\,\mathrm{Pa}$, $u_0 = 100\,\mathrm{m\ s^{-1}}$, $v_0 = 10^{-4}\mathrm{m\ s^{-1}}$, $T_{max} = 11\,000\,\mathrm{K}$, $T_{min} = 350\,\mathrm{K}$, $E_0 = 1\,\mathrm{V\ m^{-1}}$ and

$$f(z,r) = \left(\frac{r}{R}\right)^2 \exp\left(-\frac{z}{L} - \frac{r}{R_1}\right) \tag{46}$$

We assumed a perfect gas law. The gas constant is $\mathcal{R} = 287\,\mathrm{J\ kg^{-1}\ K^{-1}}$, the heat conductivity is $k = 3.54\,\mathrm{W\ m^{-1}\ K^{-1}}$, the dynamic viscosity is $\mu = 1.25 \times 10^{-4}\mathrm{Pa\ s}$ and the heat capacity ratio is $\gamma = 1.46$. The electric field produced by the coil has been turned off. The electric conductivity of the air is supposed to be $\sigma = 3804.7\,\mathrm{S\ m^{-1}}$ in the ICP domain, but null in the Maxwell domain. The induction frequency is $f = 0.37\,\mathrm{MHz}$.

4.1.2. Mesh convergence study

High-order methods using polynomial degree p converge in the L_2 norm to the analytical solution $\mathbf{u}^*$ of the problem with order $p+1$ with the mesh size h. The mesh used here is unstructured and refined uniformly. The convergence graphs of the ICP

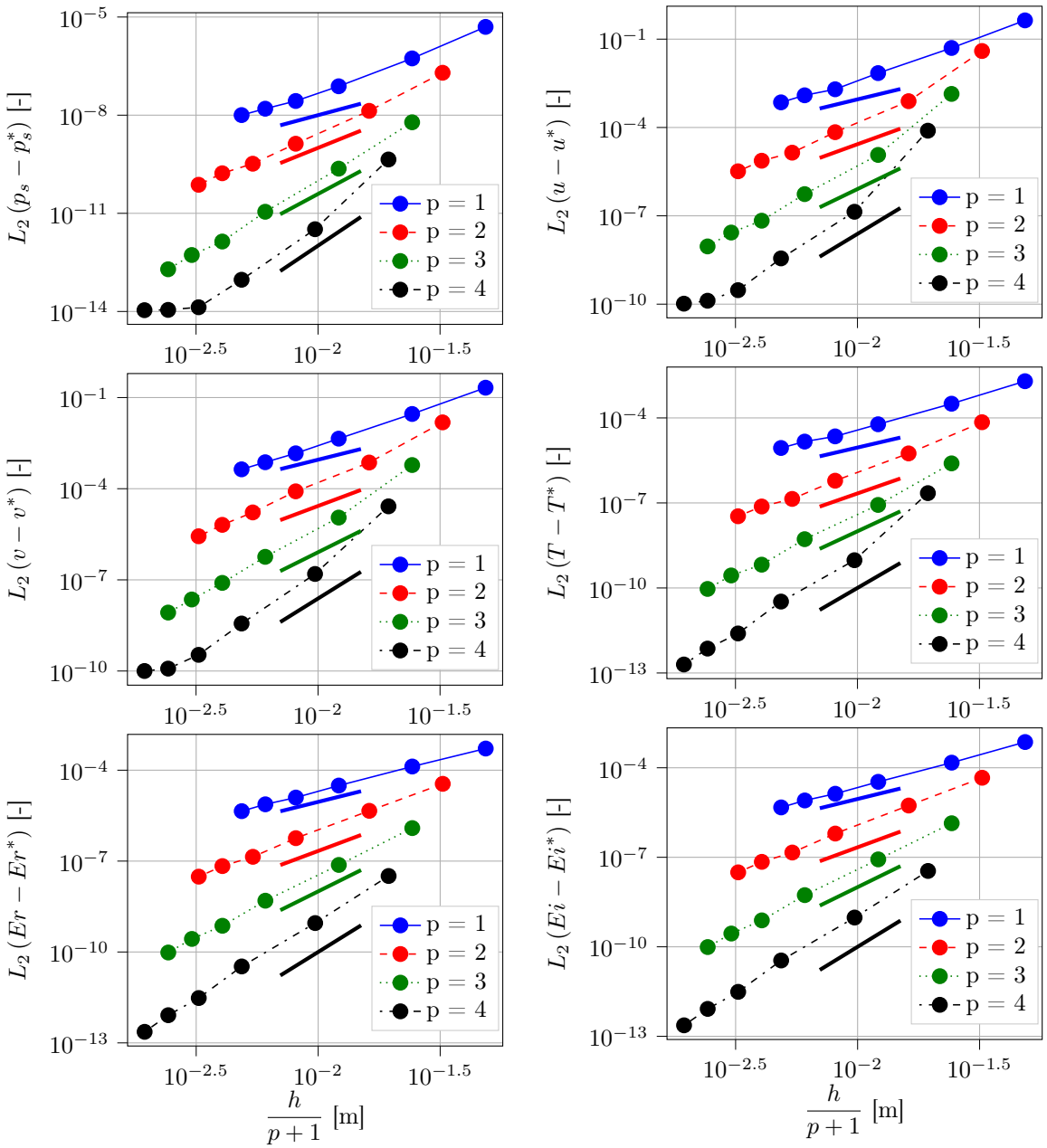

Figure 5: Convergence of the L_2 norm of the error on the static pressure p_s, velocities u, v, temperature T and real and imaginary electric Er, Ei fields respectively in the ICP domain as a function of the mesh size h divided by $p+1$, with p the order of the method. The quantities have been made dimensionless using their characteristic values. The thick lines are of slope $p+1$ and serve as comparison with the expected order of convergence.

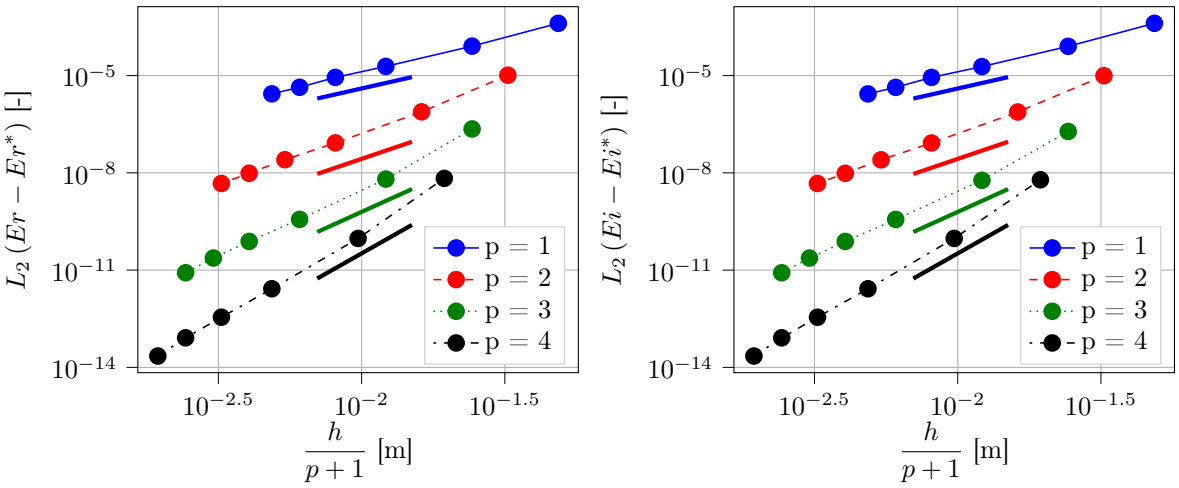

Figure 6: Convergence of the L_2 norm of the error on the real Er and imaginary Ei electric fields respectively in the Maxwell domain as a function of the mesh size h. The quantities have been made dimensionless using their characteristic values. The thick lines are of slope $p+1$ and serve as comparison with the expected order of convergence.

part of the domain are given in Fig. 5, while the Maxwell part is given in Fig. 6. The expected convergence order of $p+1$ are retrieved. The previous results indicate that the implemented multi-domain HDG method for inductively coupled plasma converges with the expected order to the solution. The next steps are the verification with COOLFluiD and the validation with experimental data.

4.2. Comparison of HDG and FV codes for ICP simulations

We compare the ICP results obtained from the HDG and the COOLFluiD solvers for the test case presented in Fig. 7, where the chamber contains a hemispherical probe.

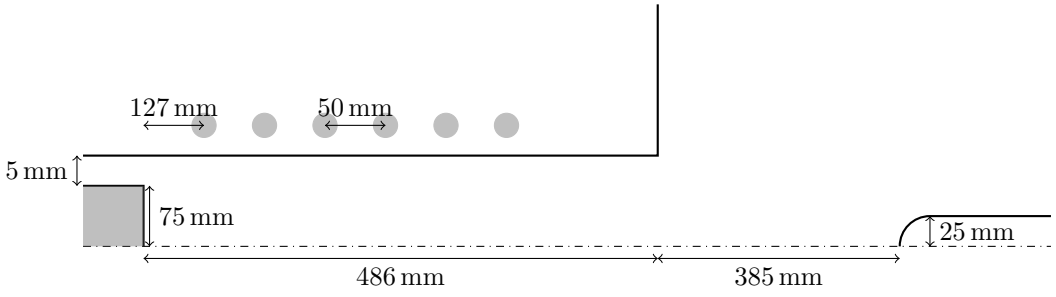

Figure 7: Schematic representation of the Plasmatron ICP torch (not at scale). The geometry is axisymmetric. The coils surrounding the facility are located at the center of the grey disks on the schematic.

The flow parameters are

- Coil induction frequency $f = 0.37\,\text{MHz}$,

- Inlet mass flux $Q = 16\,\mathrm{g\,s^{-1}}$,
- Background pressure $p_0 = 5000\,\mathrm{Pa}$,
- Power dissipated in the facility $P = 100\,\mathrm{kW}$,
- Wall temperature $T_{wall} = 350\,\mathrm{K}$.

The boundary conditions are located exactly as in Fig. 1. Their definitions can be found in Section 2.4.1, with the following parameters

- The inlet velocity U_{in} is computed using the mass flow rate Q,

$$U_{in} = \frac{Q}{\rho_{in}\pi(R_2^2 - R_1^2)} = 132.8\,\mathrm{m\,s^{-1}}, \tag{47}$$

  where $\rho_{in} = 0.0496\,\mathrm{kg\,m^{-3}}$ is the density of the inlet, computed for the pressure p_0 and the inlet temperature $T_{in} = 350\,\mathrm{K}$ using the LTE table of states. $R_2 = 8\,\mathrm{cm}$ and $R_1 = 7.5\,\mathrm{cm}$ are the outer and inner radius of the annular injector.
- The stabilizing coflow is set to be $u_{coflow} = 50\,\mathrm{m\,s^{-1}}$,
- The opening outlet pressure is the same as the backgroud pressure $p_{out} = p_0$.

The remaining BC are explicitly defined in Section 2.4.1. On the other hand, the initial data are presented in Section 2.4.2:

- The initial velocity profile is the same one as the inlet

$$v_{z,inital} = U_{in} \tag{48}$$

  while the radial velocity is null.
- The temperature field has an analytical expression given in Section 2.4.2, with parameters $T_{initial} = 10\,000\,\mathrm{K}$, $T_{wall} = 350\,\mathrm{K}$ and $z_1 = 0.127\,\mathrm{m}$, $z_2 = 0.486\,\mathrm{m}$ and $z_3 = 0.8\,\mathrm{m}$.
- The pressure is set to the background pressure $p_{initial} = p_0$,
- The electric field is null in the two domains.

Finally, the conservativity condition between the Maxwell and Maxwell + Navier-Stokes subdomains translates into the conservation of the electric field numerical diffusive flux (see Eq. (34)).

The pressure, temperature, velocity and enthalpy profiles obtained using HDG ($p = 4$) and COOLFluiD (FV) along the stagnation line in front of the probe are given in Fig. 8. On the other hand, the radial profiles at distance $\Delta z = 71\,\mathrm{mm}$ and $\Delta z = 271\,\mathrm{mm}$ from the probe end are presented in Fig. 9. These graphs show a strong similarity of the CF and HDG results. The main differences occur in the velocity profile along the stagnation line, and in the pressure and velocity profiles in the radial direction. For the pressure, these differences do not exceed 0.1 Pa, which is in practice negligible. We suspect that these discrepancies come from either the difference in discretization of the FV and HDG

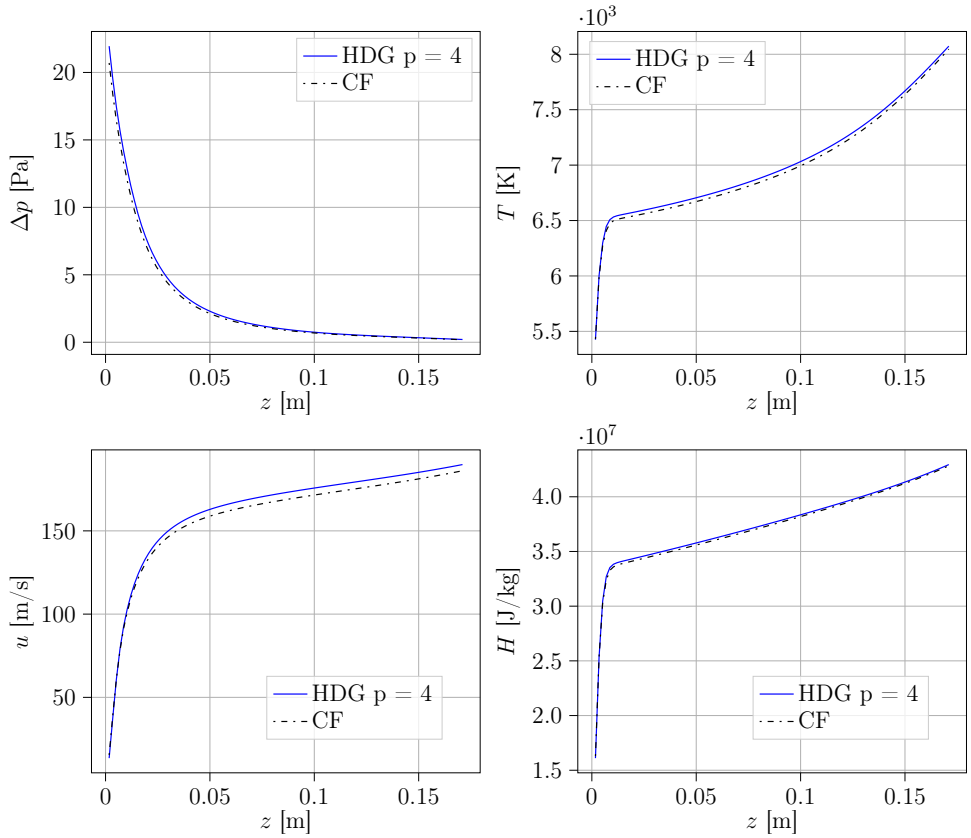

Figure 8: Comparisons of the horizontal velocity profile u, the pressure difference Δp, the temperature profile T and the enthalpy profile H along the stagnation line in front of the probe in the Plasmatron for the HDG and COOLFluiD codes. The COOLFluiD results are a private communication by E. Anfuso.

method, or in the stabilizing coflow employed. Indeed, FV being more dissipative than HDG, it requires a lower stabilizing coflow (50 m s^{-1} for HDG, 10 m s^{-1} for FV). However, these differences do not have a great impact on the enthalpy and temperature profiles. The effect of the coflow on the flow field variables should be studied, but is left for future work.

4.2.1. Mesh and L_2 norm of convergence of nonlinear solver.

The HDG mesh used for these simulations is given in Fig. 10, and is fully unstructured. This feature allows refining the mesh solely in regions of high gradients and saves DOFs elsewhere. Moreover, the high-order reconstruction permits to capture strong variations with less degrees of freedom than FV. This is particularly salient in the vicinity of the probe (Fig. 11). However, the mesh still needs to be structured and quadrangular near the boundary layers with large gradients (such as isothermal walls). It was found that triangular meshes lead to spurious oscillations in these regions [54]. This issue might result from of the coupling between the wall tangential and normal gradients

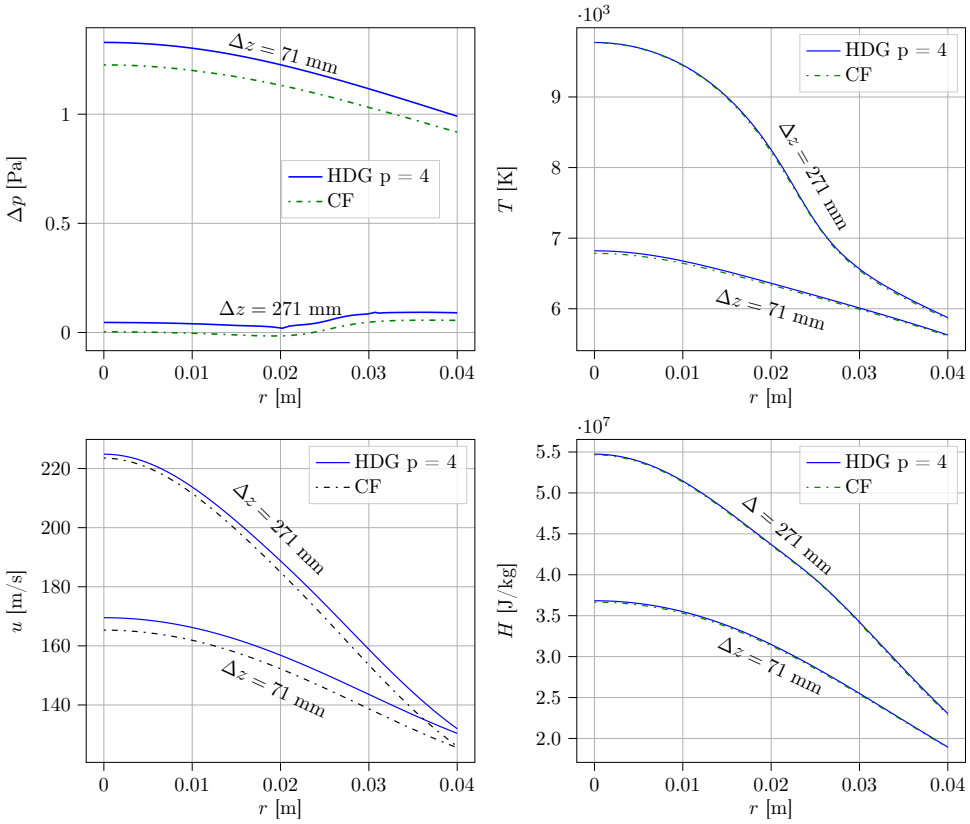

Figure 9: Comparisons of the radial velocity profile u, the pressure difference Δp, the temperature profile T and the enthalpy profile H at a position $z = 71\,\text{mm}$ and $z = 271\,\text{mm}$ from the probe front for the COOLFluiD and HDG codes. The COOLFluiD results are a private communication with E. Anfuso.

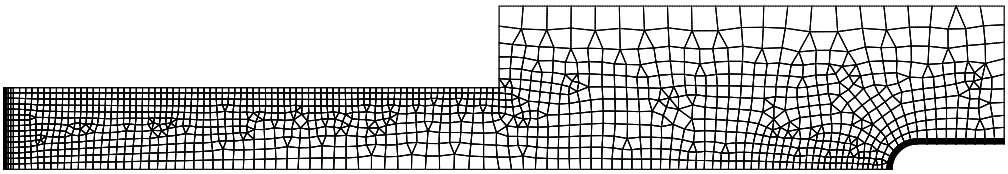

Figure 10: Mesh used for the stagnation line computations for the HDG code (above, 1588 unstructured elements in total). The electric part has been omitted.

introduced by the triangular finite element space. The problem is completely cured when the boundary layer mesh is structured with quads.

The number of DOFs for HDG is 88 520, and the convergence history of the L_2 norm of the residual is given in Fig. 12. When run on a single process and thread, the HDG code computes the solution in 25 min at $p = 4$. The solution procedure is in two steps: first, the various fields are set as described in Section 2.4 and the solver is run at order 2. Then, once the solution is converged, it is used as initial data for an order 4 simulation.

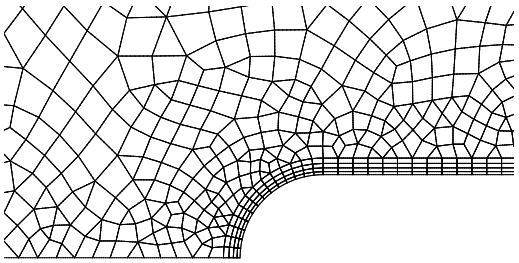

Figure 11: Mesh in the vicinity of the probe used for the HDG code which his of the order of $0.1 - 1$mm. As a comparison, typical FV mesh in the boundary layer has to be much more refined in order to capture the gradient properly (1 µm).

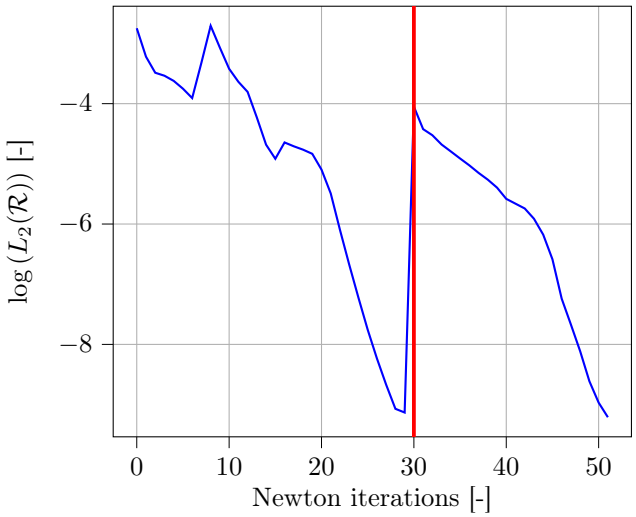

Figure 12: Convergence history of the L_2 norm of the residual $\mathcal{R}$ for the ICP code. The red vertical line represents the passage from an order 2 to an order 4 solution.

During the simulation, the CFL is monitored following Eq. (36). These procedures are fully automated. Moreover, the HDG solver requires only to use a Newton solver and does not need to use a Picard iteration to start the simulation, as required by legacy codes [43, 16].

4.2.2. Fields in the torch

The temperature and velocity fields obtained with the HDG code are shown in Fig. 13. The temperature is maximal close to the axis of symmetry of the torch. Large temperature gradients occur close to the inlet, the probe and the walls of the facility. The streamlines show a recirculation close to the annular injection. The role of this recirculation is to stabilize the torch. It also recirculates the heat produced by induction towards the inlet, creating the large temperature gradients observed close to the inlet wall. The power dissipated in the facility is maximal where the coupling between the electric field and the plasma is the highest, more or less at equidistance from the centerline and the

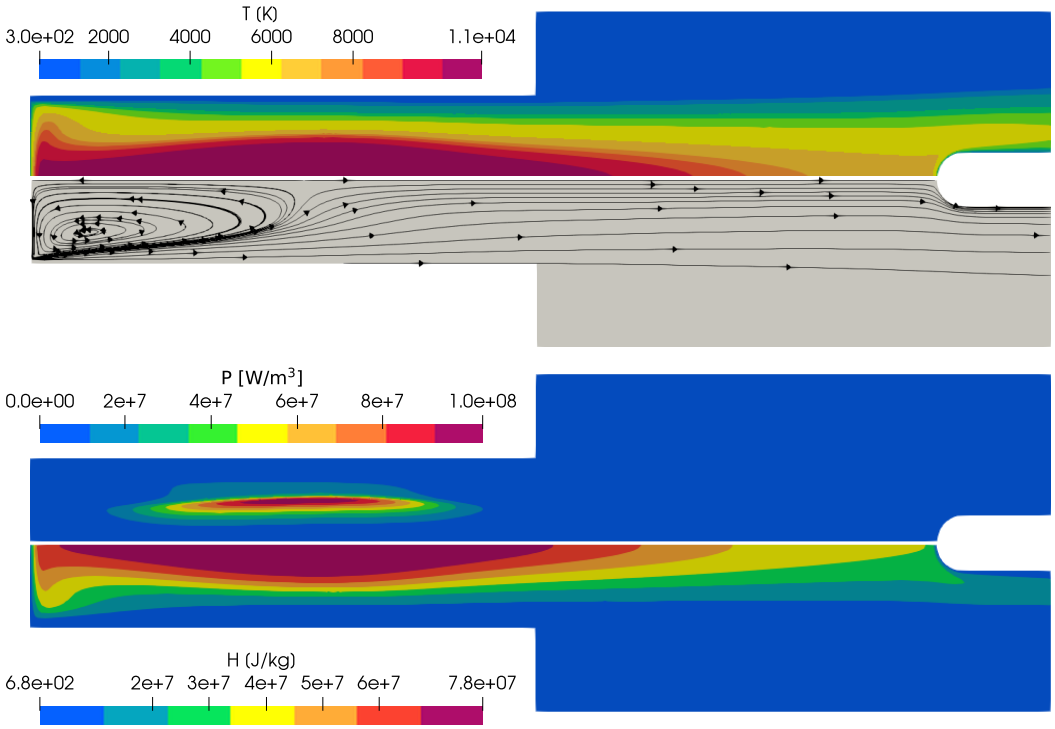

Figure 13: From top to bottom: temperature field, streamlines, power dissipated in the facility and enthalpy obtained with the HDG code in the torch and in the chamber.

torch radius. Finally, the norm of the total electric field E_{tot} is presented in Fig. 14, with $E_{tot} = \sqrt{E_{I,Re}^2 + E_{I,Im}^2}$, where $E_I = E_C + E_p$ is the induced electric field, sum of the coil and the plasma contributions. It is maximal close to the coil and decreases towards the axis of symmetry.

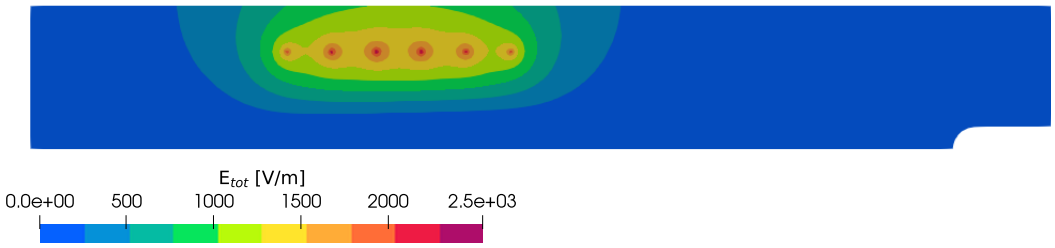

Figure 14: Total electric field E_{tot} in the facility. The electric field produced by the coil has been capped near the coil as the analytical solution is infinite at the coil location. The field is represented in both computational domains (ICP and Maxwell).

4.3. Comparison of HDG with experimental data

The HDG code results are compared to experimental data obtained in the Plasmatron facility. The inflow rate is $Q = 16\,\mathrm{g\,s^{-1}}$, the pressure is $p_0 = 200\,\mathrm{mbar}$ and the power dissipated in the facility is $P_{exp} = 200\,\mathrm{kW}$. The flow is in free-stream conditions, meaning no probe is placed in the chamber of the facility. It is also at thermodynamic equilibrium. The HDG code results agree very well with the experimental data (Fig. 15). Note that the power dissipated in the facility numerically ($P_{num} = 78\,\mathrm{kW}$) is very differ-

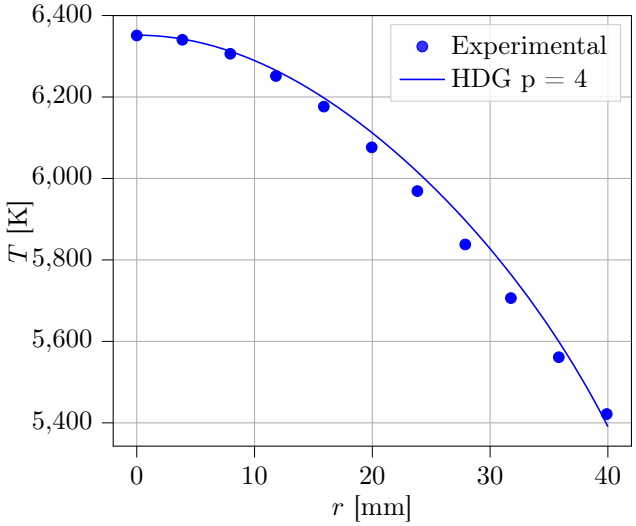

Figure 15: Comparison of the experimental radial temperature profile obtained at 385 mm from the torch exit between the symmetry axis and 40 mm. The pressure is 200 mbar, the inflow rate is $16\,\mathrm{g\,s^{-1}}$. The power actually dissipated in the facility is 200 kW, while the power injected in the numerical solver in order to match the temperature profile is 78 kW.

ent from the experimental one ($P_{exp} = 200\,\mathrm{kW}$), leading to a numerical power efficiency $\eta_{num} = P_{num}/P_{exp} \simeq 39\%$, which is very close to the results computed in [44] with COOLFluiD. This large difference between the power supplied to the generator and the power dissipated in the facility is well known in the ICP community. In order to fully estimate the loss, one must take into account the electrical circuit between the generator and the power arriving at the coil, which is the power transmitted to the facility.

5. Conclusion

In this work, we presented a monolithic multi-domain hybridized discontinuous Galerkin solver applied to inductively coupled plasma. We first showed, using a manufactured solution, that the expected order of convergence is retrieved. Then, the results obtained with the HDG code along a stagnation line in front of a probe in the Plasmatron facility were compared to results obtained using COOLFluiD. The results were in great accordance. Finally, the radial experimental temperature profile in the free-stream configuration for the Plasmatron at local thermodynamic equilibrium were compared to the HDG code, displaying a very good agreement.

In addition to reproducing results of finite volume codes, the monolithic HDG method showed a fast and robust convergence towards steady-state. Moreover, the method allowed the use of an unstructured coarse mesh. This is a strong advantage compared to FV, which requires a highly structured mesh everywhere in the computational domain and demands an extremely refined mesh in the boundary layer region. We also showed that the iterative procedure for power, previously employed in staggered solvers, can be easily and successfully adapted to monolithic strategies.

In summary, we proved that monolithic multi-domain HDG methods are better suited for the simulation of inductively coupled plasma than staggered FV methods. Looking a little further, the computational efficiency of this solver could ease the simulation of instabilities, turbulence and 3D phenomena. The exploration of non-equilibrium thermodynamics could also be investigated. These topics are left for future work.

6. Acknowledgments

The authors would like to thank the Fund for Scientific Research - FNRS, for financing this work through a Fund for Research Training in Industry and Agriculture - FRIA fellowship. They are also very grateful to Enrico Anfuso for providing the experimental results for the Plasmatron facility at the von Karman Institute for Fluid Dynamics and the COOLFluiD simulations results. Vincenzo Romano is also thanked for his participation in the COOLFluiD computations.

References

[1] E. Georg, M. I. Yakushin, Desintegrating in High-Enthalpy Air Stream, Inzhenemo Fizicheskii Zhumal 32 (4) (1977) 581–587.

[2] A. Gordeev, A. F. Kolesnikov, M. Yakushin, An Induction Plasma Application to Buran's Heat Protection Tiles Ground Tests., SAMPE journal 28 (3) (1992) 29–33.

[3] P. N. Baronets, A. F. Kolesnikov, S. N. Kubarev, I. S. Pershin, A. S. Trukhanov, M. I. Yakushin, Overequilibrium Heating of the Surface of a Heat-Shield Tile in a Subsonic Jet of Dissociated Air., Fluid Dynamics 26 (3) (1991) 437–442.

[4] N. Bykova, S. Vasil'evskii, A. Gordeev, A. Kolesnikov, I. Pershin, M. Yakushin, Determination of the Effective Probabilities of Catalytic Reactions on the Surfaces of Heat Shield Materials in Dissociated Carbon Dioxide Flows., Fluid Dynamics 32 (6) (1997) 876–886.

[5] M. Auweter-Kurtz, H. Kurtz, A. Gordeev, S. Laure, Plasma Generators for Re-entry Simulation., Journal of Propulsion and Power 12 (6) (1996) 1053–1061.

[6] M. Dropmann, G. Herdrich, R. Laufer, D. Puckert, H. Fulge, S. Fasoulas, J. Schmoke, M. Cook, T. Hyde, A new inductively driven plasma generator (ipg6)—setup and initial experiments, IEEE Transactions on Plasma Science 41 (2013) 804–810.

[7] C. Rond, A. Bultel, P. Boubert, B. Chéron, Spectroscopic measurements of nonequilibrium co2 plasma in rf torch, Chemical Physics 354 (1) (2008) 16–26.

[8] M. E. MacDonald, C. M. Jacobs, C. O. Laux, F. Zander, R. G. Morgan, Measurements of air plasma/ablator interactions in an inductively coupled plasma torch, Journal of Thermophysics and Heat Transfer 29 (1) (2015) 12–23.

[9] O. Chazot, D. Vanden Abeele, M. Carbonaro, Comparison of experimental and numerical results for the dynamic pressure in an inductive plasma flow, Annals of the New York Academy of Sciences 891 (1999) 368 – 376.

[10] W. Owens, D. Merkel, F. Sansoz, D. Fletcher, Fracture behavior of woven silicon carbide fibers exposed to high-temperature nitrogen and oxygen plasmas, Journal of the American Ceramic Society 98 (12) (2015) 4003–4009.

[11] D. Fries, S. Stark, J. Murray, R. Bhakta, E. Jans, N. Clemens, P. Varghese, S. Kearney, Nitrogen thermometry in an inductively coupled plasma torch using broadband nanosecond coherent anti-stokes raman scattering, Applied Optics 62 (2023).

[12] L. Capponi, T. Oldham, M. Konnik, K. Stephani, D. J. Bodony, M. Panesi, G. S. Elliott, F. Panerai, Aerothermal characterization of the plasmatron x wind tunnel: Heat flux, stagnation pressure and jet unsteadiness, in: AIAA SciTech forum, 2023.

[13] M. I. Boulos, Flow and temperature fields in the fire-ball of an inductively coupled plasma, IEEE Transactions on Plasma Science 4 (1) (1976) 28–39.

[14] A. Gaillat, R. M. Barnes, P. Proulx, M. I. Boulos, Computer modeling of enclosed inductively coupled plasma discharges, Spectrochimica Acta Part B: Atomic Spectroscopy 50 (10) (1995) 1187–1205.

[15] D. Vanden Abeele, G. Degrez, Efficient computational model for inductive plasma flows, AIAA journal 38 (2) (2000) 234–242.

[16] T. Magin, A Model for Inductive Plasma Wind Tunnels, Ph.D. thesis, von Karman Institute for Fluid Dynamics (2004).

[17] A. Lani, T. Quintino, D. Kimpe, H. Deconinck, S. Vandewalle, S. Poedts, Reusable object-oriented solutions for numerical simulation of pdes in a high performance environment, Scientific Programming 14 (2) (2006).

[18] A. Lani, N. Villedieu, K. Bensassi, L. Kapa, M. Vymazal, M. S. Yalim, M. Panesi, COOLFluiD: An open computational platform for multi-physics simulation and research, 21st AIAA Computational Fluid Dynamics Conference (2013).

[19] S. Kumar, A. Munafò, K. Stephani, D. Bodony, M. Panesi, Modeling three-dimensional magneto-hydrodynamic phenomena in inductively coupled plasma discharges, in: AIAA SciTech forum, 2024.

[20] W. Reed, T. Hill, Triangular mesh methods for the neutron transport equation, Tech. rep., Los Alamos Scientific Laboratory (1973).

[21] B. Cockburn, C. Shu, The runge–kutta discontinuous galerkin method for conservation laws v: Multidimensional systems, Journal of Computational Physics 141 (2) (1998) 199–224.

[22] D. N. Arnold, F. Brezzi, B. Cockburn, L. D. Marini, Unified Analysis of Discontinuous Galerkin Methods for Elliptic Problems., SIAM Journal of Numerical Analysis 39 (5) (2002) 1749–1779.

[23] P. Schrooyen, K. Hillewaert, T. Magin, P. Chatelain, Fully implicit discontinuous galerkin solver to

study surface and volume ablation competition in atmospheric entry flows, International Journal of Heat and Mass Transfer 103 (2016) 108–124.
[24] B. Cockburn, J. Gopalakrishnan, A characterization of hybridized mixed methods for second order elliptic problems, SIAM Journal on Numerical Analysis 42 (1) (2005) 283–301.
[25] M. Woopen, A. Balan, G. May, J. Schultz, A comparison of hybridized and standard dg methods for target-based hp-adaptive simulation of compressible flow, Computers and Fluids 98 (2014) 3–16.
[26] N. C. Nguyen, J. Peraire, B. Cockburn, An implicit high-order hybridizable discontinuous Galerkin method for linear convection-diffusion equations, Journal of Computational Physics 228 (9) (2009) 3232–3254.
[27] N. Nguyen, J. Peraire, B. Cockburn, An implicit high-order hybridizable discontinuous galerkin method for nonlinear convection–diffusion equations, Journal of Computational Physics 228 (23) (2009) 8841–8855.
[28] N. Nguyen, J. Peraire, B. Cockburn, Hybridizable Discontinuous Galerkin Methods, in: J. Hestaven, R. E.M. (Eds.), Spectral and High Order Methods for Partial Differential Equations, Springer, 2011, pp. 63–84.
[29] P. Fernandez, N. Nguyen, J. Peraire, The hybridized discontinuous galerkin method for implicit large-eddy simulation of transitional turbulent flows, Journal of Computational Physics 336 (2017) 308–329.
[30] A. Modave, T. Chaumont-Frelet, A hybridizable discontinuous galerkin method with characteristic variables for helmholtz problems, Journal of Computational Physics 493 (2023).
[31] M. Woopen, A. Balan, G. May, A unifying computational framework for adaptive high-order finite element methods, in: 22nd AIAA Computational Fluid Dynamics Conference, 2015.
[32] M. Giles, Stability analysis of numerical interface conditions in fluid-structure thermal analysis, International Journal for Numerical Methods in Fluids 25 (2000).
[33] T. Verstraete, S. Scholl, Stability analysis of partitioned methods for predicting conjugate heat transfer, International Journal of Heat and Mass Transfer 101 (2016) 852–869.
[34] P. Schrooyen, K. Hillewaert, T. Magin, P. Chatelain, Fully implicit discontinuous galerkin solver to study surface and volume ablation competition in atmospheric entry flows, International Journal of Heat and Mass Transfer 103 (2016) 108–124.
[35] Z. Cai, B. Thornber, A high-order discontinuous galerkin method for simulating incompressible fluid-thermal-structural interaction problems, International Journal of Heat and Fluid Flow 83 (2020).
[36] P. Rini, Analysis of differential diffusion phenomena in high enthalpy flows, with application to thermal protection material testing in icp facilities, Ph.D. thesis, Université Libre de Bruxelles, Faculté des sciences appliquées (2006).
[37] D. Bernardi, V. Colombo, E. Ghedini, A. Mentrelli, Three-dimensional modeling of inductively coupled plasma torches, Pure and Applied Chemistry 77 (2) (2005) 359–372.
[38] T. Jang, Y. K. Seo, S. H. Sohn, J. W. Jung, Calculation of the off-axes magnetic field for finite-length solenoids, New Physics: Sae Mulli 70 (8) (2020) 667–674.
[39] N. Corthouts, Development of an axisymmetric hybridized discontinous galerkin solver for inductively coupled plasma, Master's thesis, von Karman Institute for Fluid Dynamics, Rhode-Saint-Genèse, Belgium (2020).
[40] S. Karl, D. Fletcher, G. Degrez, T. Magin, M. Playe, Assessment of radiative transport in an argon plasma flow, in: 4th European Symposium Aerothermodynamics for Space Applications, 2001.
[41] P. Rini, D. Vanden Abeele, G. Degrez, Elemental demixing in inductively coupled air plasmas at high pressures, 37th AIAA Thermophysics Conference 20 (1) (2004).
[42] J. B. Scoggins, V. Leroy, G. Bellas-Chatzigeorgis, B. Dias, T. Magin, Mutation++: MUlticomponent Thermodynamic And Transport properties for IONized gases in C++, SoftwareX 12 (2020). arXiv:2002.01783.
[43] D. Vanden Abeele, S. A. Vasil'evskii, A. Kolesnikov, G. Degrez, B. Bottin, Code-To-Code Validation of Inductive Plasma Computations, Tech. rep., von Karman Institute for Fluid Dynamics, St. Genesius-Rode, Belgium (1999).
[44] A. Fagnani, Development of Measurement Techniques and Study of the Aerothermal Response of Space Debris Materials to Atmospheric Entry Plasmas, Ph.D. thesis, von Karman Institute for Fluid Dynamics (2023).
[45] M. Woopen, G. May, J. Schütz, Adjoint-based error estimation and mesh adaptation for hybridized discontinuous Galerkin methods, International Journal for Numerical Methods in Fluids 76 (September) (2014) 811–834.
[46] M. Dubiner, Spectral methods on triangles and other domains., Journal of Scientific Computing

6 (4) (1991) 345–390.
[47] S. Venkateswaran, L. Merkle, Analysis of preconditioning methods for the Euler and Navier-Stokes equations, in: 30th CFD Lecture Series, 1999.
[48] M. S. Liou, C. Steffen, A new flux splitting scheme, Journal of Computational Physics 23 (1993).
[49] M. S. Liou, Search for a Near-Perfect Numerical Flux Scheme, Part I: AUSM+, Nasa-Tm-106524 (1994).
[50] M. S. Liou, A sequel to AUSM, Part II: AUSM+-up for all speeds, Journal of Computational Physics 214 (1) (2006) 137–170.
[51] K. Hillewaert, Development of the Disconstinuous Galerkin Method for High-Resolution, Large Scale CFD and Acoustics in Industrial Geometries, Ph.D. thesis (2013).
[52] R. Hartmann, P. Houston, Symmetric interior penalty dg methods for the compressible navier–stokes equations i: Method formulation, International Journal of Numerical Analysis and Modeling 3 (2006) 1–20.
[53] Y. Epshteyn, B. Rivière, Estimation of penalty parameters for symmetric interior penalty galerkin methods, Journal of Computational and Applied Mathematics 206 (2) (2007) 843–872.
URL https://www.sciencedirect.com/science/article/pii/S0377042706005279
[54] N. Corthouts, K. Hillewaert, G. May, T. Magin, Hybridized discontinuous galerkin method for multiphysics problems: Application to inductively coupled plasmas, in: AIAA SCITECH 2024 Forum, AIAA, 2024.
[55] S. Balay, W. Gropp, L. C. McInnes, B. F. Smith, Petsc, the portable, extensible toolkit for scientific computation, Argonne National Laboratory 2 (17) (1998).
[56] E. Sartori, Numerical Simulation of Chemical Reactive Flows in Inductively Coupled Plamsa Windtunnels, Tech. rep. (2010).